Universidad
Carlos III de Madrid
www.uc3m.es

TESIS DOCTORAL

HIGH ORDER NUMERICAL METHODS FOR MYXOBACTERIA PATTERN FORMATION

Autor:

Ana Maria Glavan

Directores:

Dr. Luis López Bonilla

Dr. Antonio Marquina Vila

DEPARTAMENTO DE CIENCIA E INGENIERÍA DE MATERIALES E INGENIERÍA QUÍMICA

Grupo de Simulación, Modelización Numérica y Matemática Industrial

Leganés, Diciembre de 2015

Universidad
Carlos III de Madrid
www.uc3m.es

TESIS DOCTORAL

HIGH ORDER NUMERICAL METHODS FOR MYXOBACTERIA PATTERN FORMATION

Autor: Ana Maria Glavan

Directores: Dr. Luis Lopez Bonilla
Dr. Antonio Marquina Vila

Firma del Tribunal Calificador:

		Firma
Presidente:	Dra. Ana Maria Carpio Rodríguez	
Vocal:	Dr. Antonio Prados Montaño	
Secretario:	Dr. Manuel Carretero Cerrajero	

Calificación:

Leganés, de de

To my family

ACKNOWLEDGMENTS

First, I would like to express my gratitude to my advisors Prof. Luis L. Bonilla and Prof. Antonio Marquina. I am deeply indebted to Luis, this work would not have been possible without his intuition, good advices, guidance and confidence during all these years. I am very grateful to Prof. Marquina for his support during all this time and for his numerous advices. Our meetings and conversations helped me a lot to understand and interpret the numerical simulation results.

Thanks also to Prof. John Neu, for his valuable advices and for the material (movies and figures) of this work. I am grateful to him to make easier my stage in Berkeley and for his clear explanations.

I would like to express my gratitude to the Department, to all the professors from the Ph. D. Program and to all the people from the Modelling and Simulation Group.

Lastly, I would like to show my gratitude to all my family and friends.

My special thanks to Silviu for his support, during the moments of joy, but especially during the more complicated ones.

Resumen en castellano

En las colonias hambrientas de myxobacteria aparecen patrones ondulatorios antes de que las bacterias se agreguen para formar cuerpos fructíferos.

Estas ondas periódicas de densidad celular itinerante surgen como resultado de la coordinación de las reversiones celulares, a causa de un reloj interno, y por el contacto de señalización durante las colisiones bacterianas.

Nuestro principal interés en esta tesis es la aproximación numérica con alta precisión para las soluciones de los modelos matemáticos propuestos para la ondulación de las myxobacterias.

Revisamos los estudios de Igoshin y coautores [Proc. Natl. Acad. Sci, EE.UU. 98, 14913 (2001) y Phys. Rev. E 70, 041911 (2004)], que describen los patrones ondulatorios de myxobacterias como un sistema de leyes de conservación hiperbólica (cuando la difusión es cero).

Teniendo en cuenta que las propiedades de la solución de sistemas de leyes de

conservación desarrollan discontinuidades de salto y fuertes gradientes en el tiempo y el espacio, consideramos importante utilizar simuladores numéricos precisos con el fin de explicar y predecir el proceso biológico natural, que es nuestro enfoque.

Anteriormente, las pautas de este modelo se obtuvieron solamente por métodos numéricos de orden de precisión inferior y no fue posible encontrar su número de onda de forma analítica.

El esquema de esta tesis es la siguiente.

En el capítulo 1 se realiza una descripción de los objetivos de la tesis y la estructura de cada capitulo.

Capítulo 2 está dedicado a una revisión general del comportamiento biológico de las myxobacterias y sobre los modelos matemáticos que han tratado hasta ahora este tema.

En el capítulo 3 se describe en detalle el modelo matemático sobre los patrones ondulatorios de myxobacterias, debido a Igoshin y coautores.

En el capítulo 4 se hace una descripción de los métodos numéricos de alta resolución empleados en este trabajo y una explicación detallada de los algoritmos que hemos desarrollado y utilizado para las simulaciones numéricas.

También analizamos el comportamiento de las reconstrucciones hiperbólicas a trozos esencialmente no oscilatorias para nuestro problema biológico, con diferentes condiciones iniciales y varios parámetros.

Con el fin de reducir la difusión numérica y reducir las oscilaciones espurias cerca de las posibles discontinuidades de la solución de la ley de conservación hiperbólica en el caso de myxobacterias, aplicamos una nueva clase de esquemas de captura de ondas de choque de orden superior que se basan en una nueva clase de funciones limitadoras, los métodos PowerPHM y WeightedPowerENO.

En el capítulo 5 se presentan varias simulaciones numéricas para modelos matemáticos sobre el comportamiento ondulatorio de las myxobacterias. Demostramos que, en ausencia de fuentes de ruido introducidas en el modelo original, el sistema de dos ecuaciones diferenciales parciales acopladas puede reproducir el proceso de reversión. Hemos utilizado herramientas numéricas de alta precisión con el fin de mantener la amplitud de las ondas viajeras.

En el capítulo 6 se deriva una ecuación de evolución para la densidad de punto de inversión que selecciona el número de onda patrón en el límite de señalización débil. Mostramos la validez de la regla de selección resolviendo numéricamente las ecuaciones del modelo y describimos otros patrones estables en el límite de la señalización fuerte. El acoplamiento de campo medio no local tiende a perder la coherencia y a confinar los patrones. En circunstancias adecuadas, puede aniquilar los patrones dejando un estado de densidad constante a través de una transición de fase no equilibrio que recuerda a la destrucción de la sincronización en el modelo de Kuramoto.

Finalmente, en el capitulo 7 se presentan las conclusiones del trabajo.

Contents

Figures List

Chapter 1. Introduction

Rippling patterns of myxobacteria appear in starving colonies before they aggregate to form fruiting bodies. These periodic traveling cell density waves arise from the coordination of individual cell reversals, resulting from an internal clock regulating them, and from contact signaling during bacterial collisions. Our main interest in this research is the numerical approximation with high order accuracy in space of the solutions of mathematical models proposed for myxobacteria rippling. We revisit the studies of Igoshin et al [Proc. Natl. Acad. Sci, USA 98, 14913 (2001) and Phys. Rev. E 70, 041911 (2004)] which describe the rippling phenomena of myxobacteria as a system of hyperbolic conservation laws (when the diffusion is zero). Since the solution of systems of conservation laws develops jump discontinuities in time and space, it is important to use accurate numerical simulators in order to explain and predict the natural biological process, which is our approach. Previously, patterns for this model were obtained only by numerical methods of low order of accuracy and it was not possible to find their wavenumber analytically. The outline of this thesis is the following.

Chapter 2 is dedicated to an overview of biological background of myxobacteria and of related mathematical models studied until now.

In Chapter 3 we describe in detail the mathematical model of rippling myxobacteria due to Igoshin et al.

In Chapter 4 we make a description of the high accuracy numerical methods employed in this work and a detailed explanation of the algorithms that we have developed and used for the numerical simulations. We analyze the behavior of the piecewise hyperbolic schemes and weighted essentially non oscillatory reconstructions for our biological problem, with different initial conditions and parameters. In order to reduce the numerical diffusion and avoid spurious oscillations near discontinuities for the solution of myxobacteria hyperbolic conservation law, we apply a new class of high order accurate shock capturing schemes that are based on a new class of limiter functions, PowerPHM and WeightedPowerENO methods.

In Chapter 5 we present various numerical tests for mathematical models of myxobacteria rippling formation. We show that in the absence of white noise sources introduced in the original model, the hyperbolic system of two coupled partial differential equations can reproduce the reversal process on a regular basis. We use high-precision numerical tools in order to maintain the amplitude of the traveling waves.

In Chapter 6 we derive an evolution equation for the reversal point density that selects the pattern wavenumber in the weak signaling limit. We show the validity of the selection rule by solving numerically the model equations and describe other stable patterns in the strong signaling limit. The nonlocal mean-field coupling tends to decohere and confine patterns. Under appropriate circumstances, it can annihilate the patterns leaving a constant density state via a nonequilibrium phase transition reminiscent of destruction of synchronization in the Kuramoto model.

In Chapter 7 we draw our conclusions.

Chapter 2. Biological Background

2.1 Introduction

One of the most important roles of developmental biology is to understand the mechanisms that underlie the processes of morphogenesis (a biological process causing an organism to develop its shape) and pattern formation [40], [52]. A pioneer spatial model for these two processes was proposed by Alan Turing in 1952, entitled "The chemical basis of morphogenesis" [66] and later confirmed experimentally in living systems.

In most of the cases of biological systems treated by the literature, the spatio-temporal wave phenomena of pattern formation result from the initial uniform state loss of stability, and are based on reaction-diffusion equations [44]. A particular case appears in bacterial colonies (e. g. *Echerichia coli, Dictyostelium discoideum, Salmonella thyphymurium*) where we can observe *self-organized* pattern structures. Two essential factors producing this cooperative behavior are chemotaxis (motion along the chemical gradient) and haptotaxis (motion along the mechanical stress gradient) [48]. The most popular case of bacterial aggregation studies is the analysis of *D. discoideum* colonies [20], [67], [58], [47].

Unlike the slime mold *D. discoideum* colonies, where the spatial patterns are generated by intercellular communication based on diffusion of the cAMP attractant [6], the density waves observed in *Myxoccocus xanthus* (a class of myxobacteria family) arise by *direct cell contacts* [22], [59]. The present study dedicates to the wave pattern formation modeling of this last class of bacteria.

Myxobacteria presents a unique life cycle and this makes it an excellent and simple model to study the development and the morphogenesis of cellular organisms. The specificity of these bacteria is that, on one hand side, they can be viewed as micropredators, because they are very efficient in killing and decomposing other microorganisms. On the other hand, they do not completely rely on living organisms, and from this point of view one can treat them as scavengers [49].

In general, the process of bacteria pattern formation is the result of the local interaction and the environmental conditions. Bacteria are forming patterns through chemotaxis, growth, and/or cells death.

However, in the case of myxobacteria, the pattern formation phenomenon arises in a different manner. Under specific conditions (when nutrients are missing), it starts the cell aggregation, transforming the surface in a pattern of bacteria density propagation, called ripples.

The rippling phenomenon is different from everything that has been encountered until this point for the reaction-diffusion systems in biology, chemistry or physics, where the waves are destroyed when they are chocking [22].

This phenomenon is it interesting not just from the biological point of view, but it acts as a pioneer problem for answering the question of how cells are interacting in order to build very organized structures, as Stevens (2000) [65] noticed. Also, this is relevant for the morphogenesis process, where the cells are cooperating and they are differentiating in order to form a new organism.

2.2 Myxobacteria: an Overview

As noticed by Shimkets et al (2006) [55], one can distinguish two metabolic groups of myxobacteria: i) cellulolytic (decomposing cellulose), e.g. *Sorangium cellulosum*, and the most frequent and also most studied category ii) proteolytic (hydrolyze proteins), e.g. *Myxococcus xanthus.*

Myxobacteria (around 50 known species, divided into 17 genera) are rod-shaped gram-negative bacteria, components of soil, that move by gliding in the direction of their long axis on solid surfaces, as individuals or in swarms [19]. In its vegetative state, myxobacteria are flexible cylinders 3-6μm long and 0.7 μm wide [55].

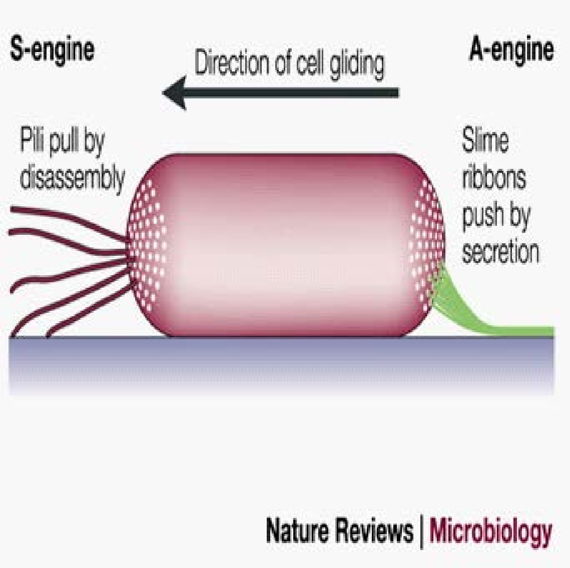

Fig 2.1: Schematic picture of the motility of myxobacteria from Kaiser (2003) [28]

Gliding speed of myxobacteria is around 1–13 $\mu m \cdot \min^{-1}$ [30], [25], [71]. This type of motility of *M. xanthus* cells is controlled by two different motors concentrated at the cell poles: the A-motility system (adventurous), specific for individual cell motion and the S-motility system (social), for group cell motion. The A-engine is a 'pusher' and works by secretion and hydration of slime, a polielectrolyte gel, whereas the S-engine is a 'puller' and operates through extension and retraction of type IV pili [69] (see Figure 2.1).

The change in the gliding direction is realized through the switching of the polarity of its two motors, and this switching is possible due to the migration of a motility protein (FrzS) across poles [43]. However, the gliding motility is it still a subject of debate, and the literature identifies two new possible causes for it, the focal adhesion mechanism and the helical rotor mechanism [5]. Due to their mix of computational modeling, imaging, and force microscopy investigation, Balagam et al (2014) [5] found evidence that the key ingredient of the focal adhesion mechanism is the elastic coupling.

During vegetative growth, when nutrients are abundant, myxobacteria aggregate into multicellular swarms and spread outwards the border of the colony where prey other bacteria as a nutrient by lysing with secreted exoenzymes [50]. In response to starvation conditions, cells stop swarming outwards and change their direction through the center of the colony, beginning a developmental cycle which culminates with the multicellular fruiting body formation with nonmotile spores. These spores can survive for long periods of time and under the adequate conditions germinate giving rise to motile vegetative cells [33]. Fruiting body is a multi-step process of alignment, rippling, streaming, and aggregation. An experimental illustration of the life cycle of the myxobacteria is shown in Figure 2.2.

In Figure 2.3, some cells have been marked with a fluorescent color, and even if it seems that each cell was waving, it was only the cells density that was presenting the wave propagation phenomenon [59].

The collective motion of myxobacteria during the biological morphogenesis having the result the fruiting bodies formation acts as a relatively simple replica of multicellular organization in higher organisms. Despite its simplicity, the formation of

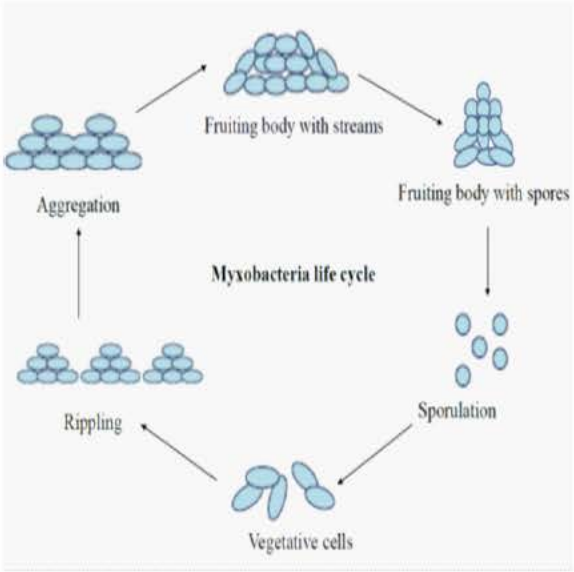

Fig 2.2: Illustration of the myxobacteria life-cycle

myxobacteria patterns is still not completely understood, but recent studies show that the aggregations during the myxobacteria development can be caused by head-to-tail interactions between cells [24].

Before aggregation begins, bacterial collective behavior and intercellular communication create fascinating collective concentric and spiral traveling waves called *ripples* (see Figure 2.4).

These ripples consist of equispaced dense ridges of high cell density which appear to advance through the population as rhythmically traveling waves that move in opposite directions. In these counter-propagating waves, individual cells are parallel

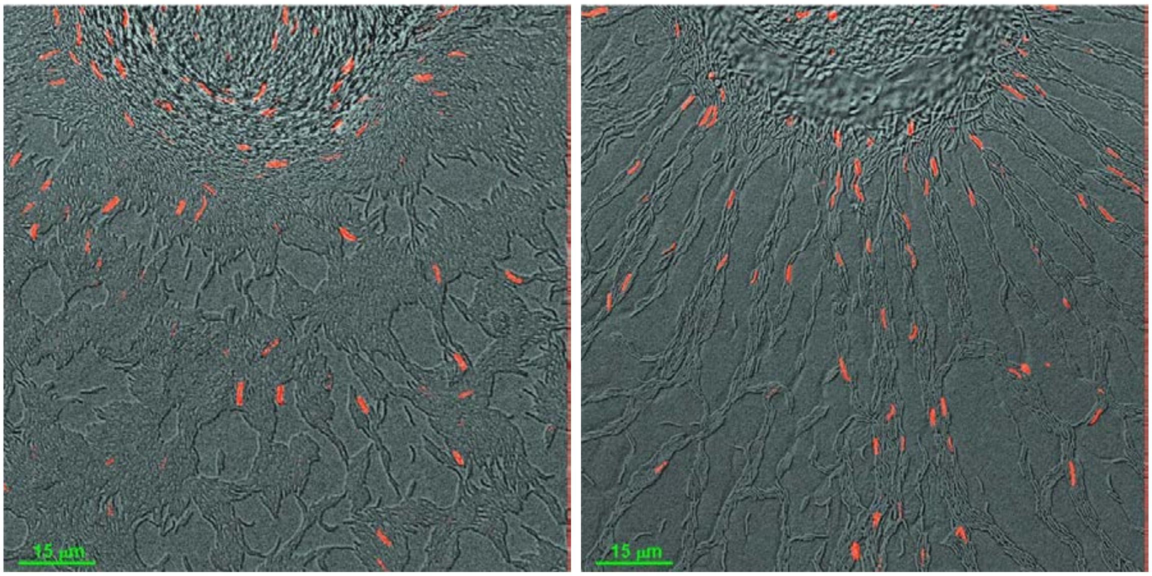

(a) Fruiting body with ripples (b) Fruiting body with streams

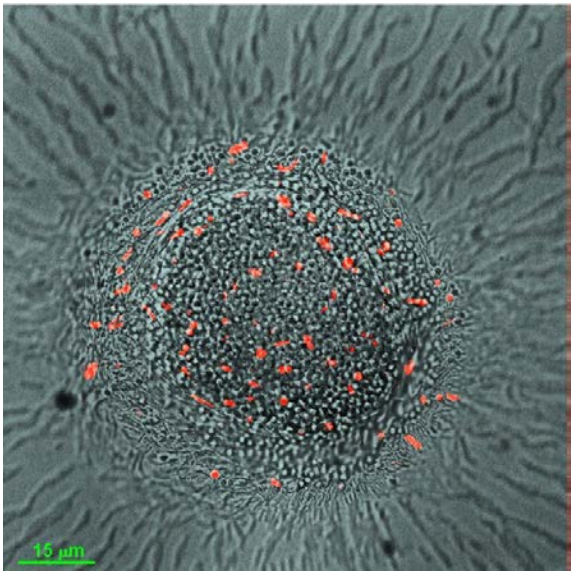

(c) Fruiting body with spores

Fig 2.3: A monolayer culture, where the individual cells are fluorescently tagged. Stages of fruiting body myxobacteria development. (a) Fruiting body with ripples; (b) Fruiting body with streams; (c) Fruiting body with spores. Reproduced with the permission of O. Sliusarenko [60]

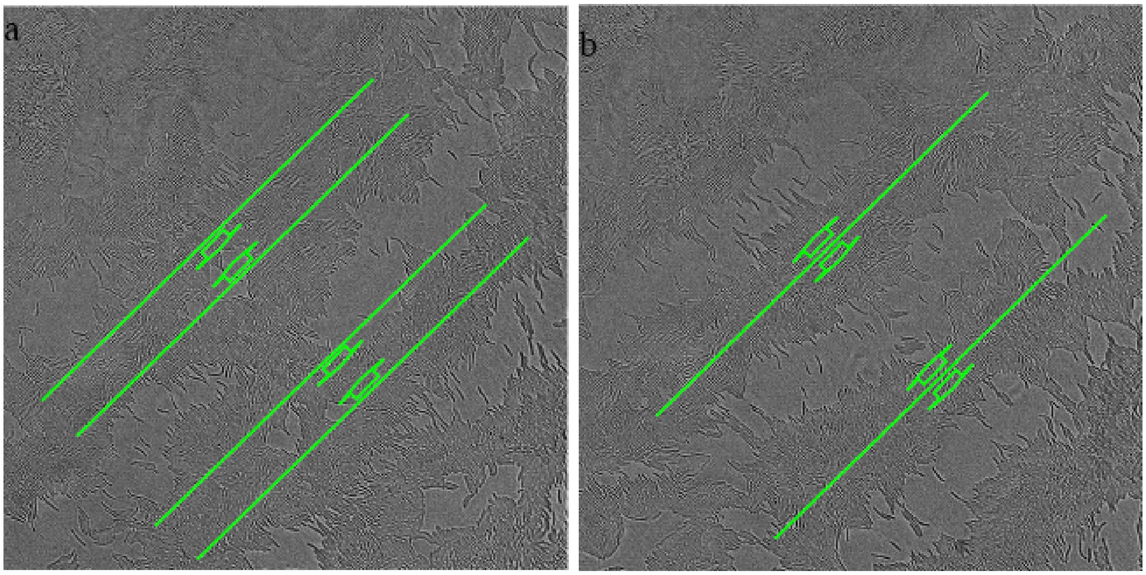

(a) Before collision (b) During collision

Fig 2.4: Schematic picture of myxobacteria ripples in the monolayer culture from O. Sliusarenko where the individual cells are fluorescently tagged: a) Before collision. b) During collision. The waves oscillate back and forth in the directions marked by the arrows. Reproduced with the permission of O. Sliusarenko [60] with the direction of ripples and move back and forth and exchange developmental signals (C-signal) [34], [9], [26]. Most experimentally observed rippling patterns [51], [68] can be characterized as counter-propagating traveling waves. Unlike any other waves generated by diffusion-reaction systems from biology, chemistry or physics, the density waves observed in myxobacteria pattern formation are analogous to solitons [22].

2.3 Theoretical Models

In order to qualitatively reproduce the myxobacteria morphogenesis mechanism, several theoretical models have been developed based on different assumptions. There are two types of mathematical models, namely the continuous and the discrete ones.

The continuous models are often treating the bacteria like a colony density modeled with the aid of partial differential or integro-differential equations.

Continuous models, *e.g.* Igoshin et al (2001) [21], Igoshin et al (2004) [22], Lutscher and Stevens (2002) [39], or more recently Harvey et al (2013) [16], study the formation of the rippling patterns observed in myxobacteria populations.

The models of Igoshin et al [21], [22], which are the starting point of this research, are formulated in terms of a continuous cell density function, that in turn depends on three parameters: space, phase (the internal biochemical clock), and time. The main assumptions of this model are the fundamental role of C-signaling for the pattern formation and the presence of the refractory period.

Lutscher and Stevens (2002) [39] model is based on a one-dimensional hyperbolic system of Goldstein-Kac type with density-dependent coefficients, where the turning rates are described in terms of reaction kinetics. In this model it is not needed the existence of a refractory period, but it requires the nonlinear dependence of C-signaling on cell density like in the Igoshin et al (2001) [21].

A multiphase hydrodynamic continuum model proposed by Harvey et al (2013) [16] is coupling the densities of oriented and isotropic phases of myxobacteria and analyzes the instability leading to the spontaneous formation of moving cell clusters.

On the other hand side, other studies use models in which space, time or state may be discrete (the discrete models). Two main categories of models are the lattice-based ones and the off-lattice node-based Monte-Carlo models.

In lattice-based models, like Stevens (2000) [65], Alber et al (2004) [2], Sozinova et al (2005) [62], Sozinova et al (2006) [63], the space is discrete and cells are situated in finite lattice sites according to local rules and undergo state changes when they collide. These state changes can be stochastic or deterministic.

A simple stochastic cellular automaton model is described by Stevens (2000) [65], where the cells move on a square grid with periodic boundary conditions and respond to the four neighbors of their frontal cell poles through a chemoattractant and slime.

The simulations reveal the experimentally observed aggregation.

Another discrete model highly studied is the Lattice Gas Cellular Automaton (LGCA) model, where the space, time and state are discretized. Sozinova et al (2005) [62] develop a 3D stochastic LGCA model where they simulate two stages of cell aggregation, followed by another 3D LGCA model in [63], which reproduces all the stages of the forming fruiting body in myxobacteria.

Börner et al (2002) [8] develop a discrete cellular automaton model where the cells are represented as occupied nodes in a three-dimensional square lattice, and they interact through collisions with neighboring cells. The refractory phase after each cell reversal is necessary for the rippling process, and the duration of this phase determines the wavelength and the period of the ripple patterns.

Later, Börner and Bär (2004) [7] use a generalized discrete model based on the same assumptions as Igoshin et al (2001) [21] continuous model and Börner et al (2002) [8]. They show that the rippling patterns can appear even in the absence of the refractory phase, if the interaction strength and the degree of cooperativity are large enough.

An individual-based model is developed by Anderson et al (2005) [3] with the objective of reproducing the rippling patterns of myxobacteria. The cells are points in a continuous space, each of them having an internal clock controlling its turning behavior and the sensitivity to C-signal. They examine also the effects of C-signal strength, sensitivity/refractoriness, and cell density for the formation and structure of the rippling patterns. This model combines the advantages of the models of Igoshin et al (2001) [21] and Börner et al (2002) [8], and the behavior of individual cells is controlled by an internal clock.

In the cellular Potts model of Starruß et al (2007) [64], another lattice-based model, the cells are distributed on a lattice and interact with the neighbors via an interaction energy in the global Hamiltonian, the system's free energy, taking into account the cellular flexibility and cell configurations.

In the off-lattice node-based Monte-Carlo models the space is continuous and cells are connected to nodes changing stochastically their position (e.g. Wu et al (2007) [70], Hendrata et al (2011) [18]).

Wu et al (2007) [70] present a model based on the description of the bacterial motility engines and their regulation. They find a strong correlation between the order of collective motion and the swarming efficiency, suporting the connection between social interactions and population-level swarming behavior.

Hendrata et al (2011) [18] incorporate the Dynamic Energy Budget model into their off-lattice model, in order to control cell growth and cell division for swarming. Their A- and S-motility algorithms simulate the swarming patterns of A+S+, A+S-, and A-S+ myxobacteria cells.

Zhang et al (2012) [72] have proposed a 2D agent based model (ABM) to simulate rippling in M. xanthus. In this model, three ingredients are sufficient to generate the rippling behavior: side-to-side signaling between two cells are causing one of the cells to reverse, a minimal refractory period after each reversal is required, and physical interactions are causing the cells aligning.

Chapter 3. Myxobacteria Mathematical Model

3.1 Introduction

When starving, myxobacteria aggregate and form a fruiting body with nonmotile spores. Before aggregation begins, there appear periodic patterns of equally spaced high density bands that move as traveling waves (ripples). These waves appear from an initially homogeneous colony, reflect the local bacterial density, and display various properties [51], [68]:

-each myxobacterium cell oscillates back and forth and the wave crests move with the same velocity as individual cells.

-in wave crests, the cell density is 3-8 times bigger than in the troughs. [51]

-during the collisions, the wave crests behave like soliton waves, without interfering. [21]

-in rippling colonies, individual cells reverse periodically their direction by switching the pole ends. [68]

-as mentioned in Chapter 2, the rippling process requires two forms of motility: A-motility (adventurous) and S-motility (social). Both, A- and S-motility motors are located at the cell poles, and the reversal of direction implies switching of the motors activity from one pole to another.

-the intercellular communication depends on a cell surface protein called C-signaling and is required for rippling. The C-signals depend on end-to-end contacts and control the frequency of reversals. [28]

These properties are taken into account for the mathematical model of myxobacteria patterns from the next section.

3.2 The Model for the Myxobacteria Rippling

In this chapter we analyze the one-dimensional (1D) model of ripples of Igoshin et al [21], [22]. The model represents the internal biochemical cycle of the rippling phase describing the motion of myxobacteria to produce a periodic pattern of traveling cell density waves and is based on the following experimental observations:

- *Internal biochemical clock*: cells are aligned parallel and glide along their long axis in one direction during part of their internal period and glide in the opposite direction during the other part of their period.

- *Contact signaling*: a cell collides with an oppositely moving cell and interchanges a signal (a C-protein). As a result, both cells reverse their motion. The collision frequency depends on the local cell density.

- *Refractory period*: after one collision there is a refractory period during which the cell does not reverse its motion even if it collides again.

Let $n(x, \phi, t)$ be the number density of bacteria per unit length x and per unit internal phase ϕ. Cells with $0 < \phi < \pi$ move to the right with velocity v and cells with $-\pi < \phi < 0$ move to the left (velocity $-v$). Cell division and death are negligible during the rippling phase. The governing equation is as follows:

$$\partial_t n + v(\phi)\partial_x n - D_x \partial_x^2 n + \partial_\phi J(x, \phi, t) = 0, \tag{3.1}$$

$$v(\phi) = v \,\mathrm{sign}\phi. \tag{3.2}$$

Here $D_x \geq 0$ is a space diffusivity, the density $n(x, \phi, t)$ is a 2π-periodic function of ϕ and it satisfies periodic boundary conditions at $x = \pm L$ or it decays to zero if $L = \infty$. To model the angular flux $J(x, \phi, t)$, we make precise the above experimental observations [22]. The cell velocity is given by (3.2) and reversals occur at $\phi = 0, \pm\pi$. The internal clock of a bacterium advances with constant angular velocity ω but when the cell collides with another one moving in the opposite direction, both cells exchange a signal. The collision frequency, and therefore the signaling intensity, is proportional to the local cell density. The cells may respond positively to this signal by accelerating their angular speed from ω to $\omega + \epsilon\omega\Omega(N_\pm)$ (see below) depending on their internal phase. The coefficient ϵ measures the relative change in angular velocity from that during the refractory period, ω, to the bacterium velocity during the signaling period, thereby characterizing signaling strength. After each reversal (at $\phi = 0, \pm\pi$), the cell enters a refractory period during which does not respond to collision signaling and does not reverse. If $\alpha > 0$ is the angular duration of the refractory period, the angular flux is $J = \omega\, n(x, \phi, t)$ for $0 < \phi < \alpha$ and for $-\pi < \phi < -\pi + \alpha$ $(0 \leq \alpha \leq \pi)$. Overall the angular flux is [22]

$$J = \omega\, n\,[1 + \epsilon\Omega(N_-(x,t))\chi_{[\alpha,\pi]}(\phi) + \epsilon\Omega(N_+(x,t))\chi_{[-\pi+\alpha,0]}(\phi)] - D_\phi \partial_\phi n, \tag{3.3}$$

$$\chi_{[A,B]}(\phi) = \begin{cases} 1, & A < \phi < B, \\ 0, & \text{otherwise}, \end{cases} \tag{3.4}$$

where

$$N_+(x,t) = \int_0^\pi n(x,\phi,t)\, d\phi, \quad N_-(x,t) = \int_{-\pi}^0 n(x,\phi,t)\, d\phi, \tag{3.5}$$

D_ϕ is a positive number and

$$\Omega(N) = \frac{N^r}{N^r + N_{\text{cr}}^r}, \tag{3.6}$$

with $r > 0$. We shall use $r = 4$ [22]. In [22], it is explained that both D_x and D_ϕ are small. The total density of bacteria at point x and time t is $N_+(x,t) + N_-(x,t)$ and the density of time-reversal points (*reversal point density*) is

$$n_{\text{RPD}}(x,t) = n(x, \phi = 0+, t) + n(x, \phi = -\pi+, t). \tag{3.7}$$

Here $n(x, \phi = 0+, t)$ and $n(x, \phi = -\pi+, t)$ are, respectively, the density of left-to-right and of right-to-left reversal points in spacetime. Thus their sum, as in (3.7), is the density of all reversal points in spacetime.

The total number of myxobacterium cells should be independent of time. This means that $dN/dt = 0$ in (3.1), where

$$N = \int_{-L}^{L} \int_{-\pi}^{\pi} n(x, \phi, t)\, dx d\phi. \tag{3.8}$$

In (3.1), n and $\partial_\phi n$ are continuous and 2π-periodic in ϕ, so that N is independent of time if and only if

$$\int_{-L}^{L} \left([J]_{\phi=-\pi}^{-\pi+\alpha} + [J]_{\phi=-\pi+\alpha}^{0} + [J]_{\phi=0}^{\alpha} + [J]_{\phi=\alpha}^{\pi} \right) dx = 0. \tag{3.9}$$

Here we have used the boundary conditions at $x = \pm L$ (including the case $L = \infty$) and the notations $[f(x, \phi)]_{\phi=-\pi}^{-\pi+\alpha} = f(x, -\pi + \alpha) - f(x, -\pi)$ and so on. For the angular flux (3.3), (3.9) becomes

$$\int_{-L}^{L} \{\Omega(N_+)\, [n]_{\phi=-\pi+\alpha}^{0} + \Omega(N_-)\, [n]_{\phi=\alpha}^{\pi}\}\, dx = 0. \tag{3.10}$$

If there is no refractory period so that $\alpha = 0$, 2π-periodicity of n and $\partial_\phi n$ yields

$$\int_{-L}^{L} [\Omega(N_+) - \Omega(N_-)]\, [n]_{\phi=0}^{\pi}\, dx = 0, \tag{3.11}$$

instead of (3.10).

It is convenient to render the equations of the model dimensionless. To this purpose, we shall use the units $[t] = 1/\omega$, $[x] = v/\omega$, etc listed in Table 3.1. Let

t	x	ϕ	$n, N_\pm$
$\frac{1}{\omega}$	$\frac{v}{\omega}$	1	$N_{\rm cr}$

Table 3.1: Nondimensional units.

us define dimensionless variables as $\hat{t} = t/[t]$, $\hat{x} = x/[x]$, and so on. Inserting these definitions in (3.1), (3.3) and (3.8) and dropping hats in the results, we obtain the following equations:

$$\partial_t n + \text{sign}(\phi)\partial_x n + \partial_\phi n = \epsilon\left\{\frac{\mathcal{D}_x}{2\pi}\partial_x^2 n + \frac{\mathcal{D}_\phi}{2\pi}\partial_\phi^2 n - \partial_\phi([\Omega(N_-)\chi_{[\alpha,\pi]} + \Omega(N_+)\chi_{[-\pi+\alpha,0]}]n)\right\}, \tag{3.12}$$

$$\int_{-\mathcal{L}}^{\mathcal{L}}\int_{-\pi}^{\pi} n(x,\phi,t)\,dx d\phi = \int_{-\mathcal{L}}^{\mathcal{L}}[N_+(x,t) + N_-(x,t)]\,dx = \hat{N}, \tag{3.13}$$

where (the dimensionless parameters are assumed to be of order unity):

$$\mathcal{D}_x = \frac{2\pi D_x \omega}{\epsilon v^2}, \quad \mathcal{D}_\phi = \frac{2\pi D_\phi}{\epsilon\omega}, \quad \mathcal{L} = \frac{\omega L}{v}, \quad \hat{N} \equiv \frac{N}{N_{\rm cr}}, \quad \Omega(y) = \frac{y^r}{y^r + 1}. \tag{3.14}$$

For $\mathcal{D}_x = \mathcal{D}_\phi = 0$, (3.12) resembles a hyperbolic equation (or a system of two hyperbolic equations for oppositely moving bacteria). However, strictly speaking this system is only hyperbolic in the spatial dimension. The phase fluxes (resulting from the nonlinear interaction between oppositely moving bacteria) are *nonlocal* in the clock angle: they are defined as integrals over the whole angular domain implying that the resulting 2D system (in x and ϕ) is integro-differential. The role of the nonlocal advection as generator of dissipation will be shown by solving (3.12) using high order accurate numerical methods in Chapter 5 and by the analysis of the weakly nonlinear limit in Chapter 6.

Chapter 4. High Order Accurate Numerical Methods

4.1 Introduction

In order to be able to correctly predict the biological phenomena such as traveling waves pattern of myxobacteria described in Chapter 3, we need to apply high accuracy numerical methods.

More specific, we want to obtain high order numerical approximations to myxobacteria hyperbolic conservation law with nonlocal phase speed, applying shock capturing reconstructions used in numerical resolution of conservation laws.

The hyperbolic conservation law solution may produce discontinuities in space, and the approximation of this solution by traditional classical methods introduces spurious oscillations around discontinuities. For this reason, these solutions should be studied in a suitable weak formulation. Such a weak formulation is given by the so-called viscosity solutions. Weak solutions of nonlinear conservation laws are piecewise smooth with jump discontinuities and can be approximated by monotone schemes. A pioneer in this field is Godunov's method [12]. His idea was to solve the Riemann problem, defined at cell interfaces such as piecewise constant initial states, and computing the numerical fluxes by integration of the conservation law in each computational cell.

Although in practice (see [12], [37]) there are used numerical methods of order one or two due to their simplicity and robustness, it is a better choice to use high order methods, despite being more complicated to understand and to code, and costly to run. Their advantage is that they are giving high accuracy on smooth regions of the solution and they are reducing the numerical viscosity at discontinuities, reducing numerical diffusion and avoiding spurious oscillations. The procedure to obtain numerical methods of high accuracy is to divide the domain interval of the function into subintervals, and approximate locally the original function using an elementary function (e.g. polynomial, rational) for each subinterval.

Another way to eliminate the drawbacks of the methods of lower orders is to apply power limiter functions. The numerical schemes that are using such limiter functions are called shock capturing schemes. The first shock capturing method was Lax-Wendroff scheme [36], a non-monotone second order method who generates spurious oscillations near discontinuities. The simplest way to measure the oscillations of a scheme is to control its total variation. Harten in [13] introduced the total variation diminishing schemes to overcome the non-monotonicity for high order accurate numerical methods. To continue in the area, Osher and Chakravarty designed TVD schemes of any order of accuracy in [46]. The next step in the evolution of high order accurate reconstruction methods is to use mean limiters (i.e., minmod limiter from Van Leer method [37]) in order to avoid Gibbs' phenomena and oscillatory patterns around discontinuities. Another examples of limiter functions (ENO, minmod, harmonic) are based on a mean of a two nonnegative numbers. In [54], Serna and Marquina defined a large class of averages, bounded by the arithmetic mean, expressed by the relation

$$power_p\left(x,y\right) = \tfrac{(x+y)}{2}\left(1-\left|\tfrac{x-y}{x+y}\right|^p\right),$$

where x and y are positive, and p is a natural number. This new class of limiters are called power limiters. From here it results a piecewise hyperbolic power (Power PHM) method with no oscillations near discontinuities, eliminating the so-called smearing effect encountered in essentially non-oscillatory (ENO) methods. As we will see in the next chapter, we use this reconstruction procedure for our numerical simulations.

Liu, Osher and Chan [38] have designed the weighted essentially non-oscillatory (WENO) methods getting fourth order accuracy using a convex combination of the ENO3 cell averaged parabolas. Based on the pointwise ENO3 parabolas, Jiang and Shu developed in [27] the WENO5 method using a nonlinear convex combination of all the candidate stencils each being assigned a nonlinear weight which depends on the local smoothness of the numerical solution based on the stencil. WENO improves upon ENO in robustness, it has better smoothness of fluxes, better steady state convergence and more efficiency.

We use shock capturing methods, often employed in the computational fluid dynamics. Because the solutions of this type of equations can develop shocks, discontinuities in time etc, it is important to use high order numerical schemes in order to correctly predict the natural phenomena.

We apply two local third order accurate methods (PHM and Power PHM) by using a piecewise hyperbolic reconstruction and another two fifth order methods (WENO5 and WenoPowerENO5) by using a piecewise parabolic reconstruction. In order to show the efficiency of the previously described methods and to apply them to our problem, we will begin the numerical experiments by using the first order numerical approximation, the upwind scheme, as we will see in Chapter 5.

On the following we write a brief review of these methods, beginning with the basic notation of the nonlinear conservation law, then in Section 4.2 we describe the hyperbolic reconstructions, followed by the parabolic ones in Section 4.3, and then continue with our numerical results in the next chapters.

For a good understanding of the high order numerical methods that we use in our experiments, we introduce some basic notation and computational framework for an initial value problem

$$n_t + f\left(n\right)_x = 0 \tag{4.1}$$

$$n(x, t = 0) = n_0\left(x\right) \tag{4.2}$$

where the piecewise initial function $n_0\left(x\right)$ is periodic or compactly supported. Next, we see how can we find the numerical approximation of the weak solution of this IVP.

Let us define the computational grid $x_i = ih$ with i integer and h the spatial step, $x_{i-1/2} < x < x_{i+1/2}$ where $x_{i+1/2} = x_i + \frac{h}{2}$ is the cell interface, $m\Delta t < t < \left(m+1\right)\Delta t$ time discretization with Δt spatial step, and the computational cells are $C_i^m = \left[x_{i-1/2}, x_{i+1/2}\right] \times \left[t_m, t_{m+1}\right]$.

We want to find $n_i^m = \frac{1}{h}\int\limits_{x_{i-1/2}}^{x_{i+1/2}} n\left(x, t_m\right)dx$, a numerical approximation of the exact solution $n\left(x, t_m\right)$ of the initial value problem, in conservation form

$$n_i^{m+1} = n_i^m - \lambda\left(\widehat{f}_{i+1/2} - \widehat{f}_{i-1/2}\right) \tag{4.3}$$

where $\lambda = \frac{\Delta t}{h}$ and the numerical flux is a function of $2k$ variables

$$\widehat{f}_{i+1/2} = \widehat{f}\left(n_{i-k+1}^m, ..., n_{i+k}^m\right) \tag{4.4}$$

and is consistent with the flux (4.1),

$$\widehat{f}\left(n, ..., n\right) = f\left(n\right) \tag{4.5}$$

$\widehat{f}$ must be a Lipschitz continuous function.

Having this basic formulation of the IVP, we can use high order reconstruction procedures giving the approximation of the mean value of a piecewise smooth function $g(x)$

$$n_i^m = \frac{1}{h} \int\limits_{x_{i-1/2}}^{x_{i+1/2}} g(x, t_m)\, dx \tag{4.6}$$

associated to the grid data defined above.

Let $R_i(x)$ be an elementary function defined on C_i such that, in each computational cell, $R_i(x)$ reconstructs $g(x)$ up to some order of accuracy.

$$n_i^m = \frac{1}{h} \int\limits_{x_{i-1/2}}^{x_{i+1/2}} R_i(x, t_m)\, dx \tag{4.7}$$

When we refer to an order of accuracy reconstruction, we mean that every time $g(x)$ is smooth enough at x in C_i, then

$$g(x) - R_i(x) = O(h^n) \tag{4.8}$$

Our study refers to a first, a third and a fifth order of accuracy, and this means that for each computational cell the truncation error will have the corresponding order of accuracy.

The function $g(x)$ is smooth enough at x_i but at the interfaces it may have discontinuities, and as a consequence, $R_i(x)$ may develop Gibbs phenomena or Runge oscillatory patterns. This is one of the challenges of the numerical mathematics community, and it advocates for the necessity of the use of high order numerical reconstructions algorithms for solving different application problems.

In our numerical approximations we refer to two classes of elementary functions:

1) hyperbolas of the form

$$r_i\left(x\right) = a_i + \frac{\lambda_i}{\left(x - x_i\right) + c_i} \tag{4.9}$$

where a_i, λ_i and c_i are defined from the grid data

2) or parabolas of the form

$$p_i\left(x\right) = a_i + \left(x - x_i\right)\left[b_i + \frac{c_i}{2}\left(x - x_i\right)\right] \tag{4.10}$$

where a_i, b_i and c_i are determined from the grid data.

A numerical scheme in conservation form is called TVD (total variation diminishing), *if*

$$TV\left(n^m\right) = \sum_i \left|n_{i+1}^m - n_i^m\right| \tag{4.11}$$

then

$$TV\left(n^{m+1}\right) \leq TV\left(n^m\right) \tag{4.12}$$

for all m (for more details see Harten who introduces the notion of TVD in reference [13]).

In order to find numerical solutions of the conservation law, it is desirable to work with the discrete conservation form of the equation (4.1). In this case, by integrating the conservation law we will obtain cell averages values of the function n. The transformation of the reconstructed solution from cell averages into the reconstructed fluxes from the cell interfaces, namely from the point values, is possible due to the following lemma of Shu and Osher [57]:

LEMMA 1 *If a function* $g(x)$ *satisfies*

$$f\left(n\left(x\right)\right) = \frac{1}{h}\int\limits_{x-\frac{h}{2}}^{x+\frac{h}{2}} g\left(\xi\right) d\xi \tag{4.13}$$

then

$$\left(n\left(x\right)\right)_x = \frac{g\left(x+\frac{h}{2}\right) - g\left(x-\frac{h}{2}\right)}{h} \tag{4.14}$$

In order to implement a high order accurate numerical scheme, we start with a first order monotone scheme based on a numerical flux. Then, using the reconstruction procedure, we approximate the numerical fluxes and variables solving the equation (4.13) up to some degree of accuracy. By the reconstruction procedure we mean to compute the numerical fluxes and variables at the cell interfaces. With this procedure we use the discrete conservation form of the equation to evolve in time.

Having the approximated spatial fluxes, and in order to have the same order of accuracy for the time discretization, the entire equation is evolved in time with a method of lines using the TVD Runge-Kutta method, developed by Shu and Osher [57].

Thus, in our work, in order to solve the ordinary differential equation

$$\frac{dn}{dt} = L(n) \tag{4.15}$$

with $L(n)$ the spatial operator, we use the third-order TVD Runge-Kutta method:

$$\begin{aligned} n^{(1)} &= n^m + \Delta t L(n^m) \\ n^{(2)} &= \tfrac{3}{4}n^m + \tfrac{1}{4}n^{(1)} + \tfrac{1}{4}\Delta t L(n^{(1)}) \\ n^{m+1} &= \tfrac{1}{3}n^m + \tfrac{2}{3}n^{(2)} + \tfrac{2}{3}\Delta t L(n^{(2)}) \end{aligned} \tag{4.16}$$

In the next sections we describe the hyperbolic and parabolic reconstructions, with the adapted algorithms that we use in our numerical simulations.

4.2 Hyperbolic Reconstructions

4.2.1 Piecewise Hyperbolic Method

We use the piecewise hyperbolic method (PHM) proposed by Marquina in [41], a third order accurate shock capturing method that is local in the sense that the numerical fluxes are reconstructed from the data of four-point variables without the information of the smoothest neighboring cells. Thus, it gives better accuracy than TVD methods. The PHM upwind method is stable, not sensitive to the Courant-Friedrichs-Lewy condition and it achieves third order accuracy in smooth regions except at local extrema where it may degenerate to $O(h^{\frac{3}{2}})$, is stable in presence of discontinuities and has less viscosity than ENO schemes of the same order.

In the PHM methods the local total variation of the reconstruction $\{R\}$ is controlled by using slope limiters, preprocessing the first order derivatives without loss of accuracy (for details see [41]).

The idea is to ensure third order of accuracy in smooth regions with the elementary function R_i, such that for each computational cell, it must be satisfied the relation (4.7) and the condition,

$$d_{i+\frac{1}{2}} = \frac{n_{i+1} - n_i}{h} \tag{4.17}$$

where $d_{i+\frac{1}{2}}$ is given by the divided first-order differences or by $d_{i+\frac{1}{2}} = R'\left(x_{i+1/2}\right)$.

If there are known the first order derivatives of g, the following definition (from [41]) establishes the interpolating relation between the mentioned hyperbolas and the conditions (4.7),

$$R'\left(x_{i+1/2}\right) = g'\left(x_{i+1/2}\right), \tag{4.18}$$

$$R'\left(x_{i-1/2}\right) = g'\left(x_{i-1/2}\right), \tag{4.19}$$

ensuring third order accuracy in smooth regions.

Definition 1. We say a method of reconstruction $\{R_i\}$ *of* $g(x)$ *is local if for every* i *the function* R_i *depends only on* n_i, $d_{i-\frac{1}{2}}$ *and* $d_{i+\frac{1}{2}}$.

As we saw before, at each time step, we need to control the change in total variation of the reconstruction procedure. Following Marquina, we introduce the next definition.

Definition 2. A method of reconstruction is local total variation bounded (LTVB) if there exists a constant $M > 0$, *independent of* h, *such that*

$$LTVB_i \leq Mh \tag{4.20}$$

for all i.

From literature [53], we see that when discontinuities are present, hyperbolas are much less oscillatory than parabolas.

As we have mentioned, the first two high order accurate numerical schemes applied for obtaining the numerical solution of myxobacteria patterns are based on hyperbolic reconstructions.

We applied the third order PHM method from Marquina's study [41], where using a three point stencil, we can obtain a piecewise hyperbolic reconstruction of type (4.9).

At $i = 0$, where the spatial numerical cell is $\left[x_{-\frac{1}{2}}, x_{\frac{1}{2}}\right]$, we can fit a hyperbola $r_0\left(x\right)$ in terms of an nondimensional parameter α and of d_0. The obtained hyperbola (4.21) must satisfy the conservation law and the condition $r_0'\left(x\right) = d_0$

$$r_0\left(x\right) = n_0 + d_0 h \frac{1}{h^2}\left[\log\left(\frac{2-\alpha}{2+\alpha}\right) - \frac{\alpha h}{\alpha\left(x - x_0\right) - h}\right] \tag{4.21}$$

with the following value at the central derivative

$$d_0 = \frac{2 \cdot d_{-\frac{1}{2}} \cdot d_{\frac{1}{2}}}{d_{-\frac{1}{2}} + d_{\frac{1}{2}}} \tag{4.22}$$

Depending on the interpolation of the lateral derivatives, and for a value of d_0, there are two possible values for α:

(a) If $d_0 \cdot d_{-\frac{1}{2}} > 0$ then $\alpha = 2\left(\sqrt{\frac{d_0}{d_{-\frac{1}{2}}}} - 1\right)$ if and only if $d_{-\frac{1}{2}} = r'\left(x_0 - \frac{h}{2}\right)$

(b) If $d_0 \cdot d_{\frac{1}{2}} > 0$ then $\alpha = 2\left(1 - \sqrt{\frac{d_0}{d_{\frac{1}{2}}}}\right)$ if and only if $d_{\frac{1}{2}} = r'\left(x_0 - \frac{h}{2}\right)$. [53]

The nonoscillatory property of the reconstruction function was achieved by using the harmonic mean of the lateral derivatives, thus avoiding the enlargement of the stencil. Thus, by the algorithm of LHHR (local hyperbolic harmonic reconstruction) one can find, in each computational cell, a hyperbola r_i that interpolates the lateral derivative with the smallest absolute value; the central derivative (d_0) is the harmonic mean of lateral derivatives [41].

To ensure the LTVB property of LHHR method, the range of values of the nondimensional parameter α is

$$-2\left(\sqrt{2}-1\right) < \alpha < 2\left(\sqrt{2}-1\right) \tag{4.23}$$

In the following, we describe the algorithm for local piecewise hyperbolic reconstruction that we use, who gives the piecewise hyperbolic method (PHM). We can find a unique hyperbola r_i in every cell C_i such that $d_{i-\frac{1}{2}} \cdot d_{i+\frac{1}{2}} > 0$ satisfying $n_i = \frac{1}{h} \int\limits_{x_{i-1/2}}^{x_{i+1/2}} r_i\left(\xi\right) d\xi$ and $d_{i+\frac{1}{2}} = r_i'\left(x_{i+\frac{1}{2}}\right)$. When $d_{i-\frac{1}{2}} \cdot d_{i+\frac{1}{2}} \leq 0$, C_i becomes a transition cell.

The reconstruction procedure is for equation (4.3), and taking into account the dynamics of the differential equation, the numerical fluxes are reconstructed according to the direction of the "wind" (from the *upwind side).*

Here, for simplicity, we sketch the algorithms for a simple case, a function with one variable. However, in our numerical simulations, we find numerical fluxes of myxobacteria densities with the aid of algorithms of order three on both directions x and ϕ. For our full kinetic myxobacteria model, the 2D numerical fluxes are reconstructed using a dimension-by-dimension procedure. We compute the term $n(x_i, \phi, t)$ using one-dimensional procedure and freezing the other variable ϕ, and in an analogous way for the other dimension, by freezing the x variable.

Algorithm for PHM-LHHR

Step 1: *Computation of Grid Data*

From n_i^m we compute the grid data by means of :

$$n_i = f\left(n_i^m\right) \tag{4.24}$$

$$d_{i+\frac{1}{2}} = \frac{n_{i+1} - n_i}{h} \tag{4.25}$$

Step 2: *Local Preprocessing of Derivatives*

Computation of $d\left(i\right)$ and α_i using LHHR for all i.

Local Hyperbolic Harmonic Reconstruction (LHHR)

$tol = O(h^2)$ is the tolerance for size of divided differences

```
if ($\left|d_{-\frac{1}{2}}\right| \leqslant tol$) and ($\left|d_{\frac{1}{2}}\right| \leqslant tol$) then
    $d = 0$ and $\alpha = 0$
else
    if ($\left|d_{-\frac{1}{2}}\right| \leqslant tol$) or $\left(C_0 \text{ is a transition cell with } \left|d_{\frac{1}{2}}\right| \leq \left|d_{-\frac{1}{2}}\right|\right)$ then
        $d = 2 \cdot d_{\frac{1}{2}} \cdot \left(\frac{h^2}{1+h^2}\right)$
        $\alpha = 2 \cdot \left(\sqrt{\frac{2}{1+h^2}} - 1\right)$
    else
        if ($\left|d_{\frac{1}{2}}\right| \leqslant tol$) or $\left(C_0 \text{ is a transition cell with } \left|d_{-\frac{1}{2}}\right| \leq \left|d_{\frac{1}{2}}\right|\right)$ then
```

```
        $d = 2 \cdot d_{-\frac{1}{2}} \cdot \left(\frac{h^2}{1+h^2}\right)$
        $\alpha = -2 \cdot \left(\sqrt{\frac{2}{1+h^2}} - 1\right)$
    else
        $d = \frac{2 \cdot d_{-\frac{1}{2}} \cdot d_{\frac{1}{2}}}{d_{-\frac{1}{2}} + d_{\frac{1}{2}}}$
        if $\left|d_{-\frac{1}{2}}\right| \leq \left|d_{\frac{1}{2}}\right|$ then
            $\alpha = 2 \cdot \left(\sqrt{\frac{d}{d_{-\frac{1}{2}}}} - 1\right)$
        else
            $\alpha = 2 \cdot \left(1 - \sqrt{\frac{d}{d_{\frac{1}{2}}}}\right)$
```

With the values of $d\left(i\right)$ and α_i, one can obtain the expressions for the hyperbolas.

Step 3: **for every** i **do**

$$r\left(x_i + \frac{h}{2}\right) = n_i + d\left(i\right) \cdot h \cdot \eta\left(\alpha_i\right) \tag{4.26}$$

$$r\left(x_i - \frac{h}{2}\right) = n_i - d\left(i\right) \cdot h \cdot \eta\left(-\alpha_i\right) \tag{4.27}$$

where the function $\eta\left(\alpha\right)$ is

$$\eta\left(\alpha_i\right) = \frac{1}{\alpha^2} \cdot \left(\log\left(\frac{2-\alpha}{2+\alpha}\right) + \frac{2 \cdot \alpha}{2-\alpha}\right) \tag{4.28}$$

With these values of $r\left(x_i + \frac{h}{2}\right)$ and $r\left(x_i - \frac{h}{2}\right)$, which are the reconstructed point values at the interfaces, one can approximate the fluxes $\widehat{f}_{i+1/2}$ and $\widehat{f}_{i-1/2}$.

4.2.2 Power Piecewise Hyperbolic Method

One way to get high-order accurate reconstruction methods without spurious oscillations near discontinuities is to control the behavior of the approximation near these discontinuities using the limiter functions. A limiter function is defined as an average of two or more nonnegative numbers.

As we mentioned, in order to improve the accuracy at local extrema in the LHHR reconstruction from PHM methods, the PowerPHM method [53] applies the power limiters instead of harmonic mean to construct a three point stencil piecewise hyperbolic method. In our simulations we use the Power$_3$mean

$$Power_3\left(x, y\right) = \min\left(x, y\right) \frac{x^2+y^2+2(\max(x,y))^2}{(x+y)^2}$$

Using the power$_3$limiter, α will have a wide range of values $-2\beta \leq \alpha \leq 2\beta$ and $\sqrt{2} - 1 \leq \beta < 1$, with β positive. With this modification, one can obtain more local variation in each computational cell.

The reconstruction method is local total variation bounded (LTVB).

Next, we write the algorithm that we use in our simulations for PHM with the local hyperbolic power reconstruction (LHPR), where powereno$_3\left(x, y\right)$ limiter defines a new hyperbola in terms of d and α.

The steps of the algorithm PHM-LHPR are the same like in PHM-LHHR algorithm with the difference that the new values of $d\left(i\right)$ and α_i were obtained by:

Local Hyperbolic Power Reconstruction (LHPR)

```
Let define $tol = h^2$,
if $(d_{-\frac{1}{2}} \cdot d_{\frac{1}{2}} \leqslant 0)$ then
    $d = 0$ and $\alpha = 0$
else
    if $(\left|d_{-\frac{1}{2}}\right| \leqslant tol)$ and $(\left|d_{\frac{1}{2}}\right| \leqslant tol)$ then
    $d = \frac{d_{-\frac{1}{2}} + d_{\frac{1}{2}}}{2}$ and $\alpha = 0$
    else
        if $\left|d_{-\frac{1}{2}}\right| \leqslant tol$ then $\left|d_{-\frac{1}{2}}\right| = tol$
        if $\left|d_{\frac{1}{2}}\right| \leqslant tol$ then $\left|d_{\frac{1}{2}}\right| = tol$
        if $\left|d_{-\frac{1}{2}}\right| \leqslant \left|d_{\frac{1}{2}}\right|$ then
        $dsize = 4\left|d_{\frac{1}{2}}\right|\left|d_{-\frac{1}{2}}\right|\left(\left|d_{\frac{1}{2}}\right|^2 + \left|d_{-\frac{1}{2}}\right|^2\right) / \left(\left|d_{\frac{1}{2}}\right| + \left|d_{-\frac{1}{2}}\right|\right)^3$
            if $d_{-\frac{1}{2}} < 0$ then $d = -dsize$
```

```
        else $d = dsize$
    $\alpha = 2\left(\sqrt{dsize/\left|d_{-\frac{1}{2}}\right|} - 1\right)$
    else
        if $d_{\frac{1}{2}} < 0$ then $d = -dsize$
        else $d = dsize$
    $\alpha = 2\left(1 - \sqrt{dsize/\left|d_{\frac{1}{2}}\right|}\right)$
```

4.3 Parabolic Reconstructions

As we have mentioned before, parabolas are another elementary functions used to approximate the piecewise smooth functions with jump discontinuities. Weighted Essentially Non-Oscillatory method (WENO5) [27] and Weighted Power Essentially Non-Oscillatory method (PowerWENO) [54] are high-order accurate reconstruction procedures that are based on parabolas and we use them to approximate the weak solutions of the nonlocal hyperbolic model of myxobacteria (see Chapter 5 for numerical results). Those parabolas have the form

$$p_i\left(x\right) = a_i + \left(x - x_i\right)\left[b_i + \tfrac{c_i}{2}\left(x - x_i\right)\right]$$

where a_i, b_i, c_i are computed from the grid data.

4.3.1 WENO5 Method

Using a nonlinear convex combination of three pointwise ENO3 parabolas, Jiang and Shu developed in [27] the WENO5 method. WENO5 is a new way to measure the smoothness, by employing the indicators of smoothness. It is a method of fifth order of accuracy designed for problems with piecewise smooth solutions containing discontinuities (or shocks).

Next, we explain the algorithm of the WENO5 reconstruction that we use in our numerical simulations for myxobacteria density. From our results, we will see in the next chapter the advantages of this method in comparison with the other of lowest order of accuracy (upwind and PHM methods).

Algorithm for the WENO5 method

We compute numerical approximations at the interfaces $x_{i-\frac{1}{2}}$ and $x_{i+\frac{1}{2}}$. For our bacterial problem, the numerical fluxes for the second variable were obtained in the same way.

In our calculations we consider the following stencil points n_{i-2}, n_{i-1}, n_i, n_{i+1} and n_{i+2}, to compute the lateral derivatives at $x_{i+\frac{1}{2}}$ and $x_{i-\frac{1}{2}}$.

At the right interface $x_{i+\frac{1}{2}}$, compute the indicators of smoothness IS_0, IS_1 and IS_2 using the following expressions:

$IS_{0weno5} = \frac{13}{12}(n_{i-2} - 2n_{i-1} + n_i)^2 + \frac{1}{4}(n_{i-2} - 4n_{i-1} + 3n_i)^2$

$IS_{1weno5} = \frac{13}{12}(n_{i-1} - 2n_i + n_{i+1})^2 + \frac{1}{4}(n_{i-1} - n_{i+1})^2$

$IS_{2weno5} = \frac{13}{12}(n_i - 2n_{i+1} + n_{i+2})^2 + \frac{1}{4}(3n_i - 4n_{i+1} + n_{i+2})^2$

Then, compute the nonlinear weights w_i

$a_0 = \frac{0.1}{(\varepsilon + IS_{0weno5})^2}$; $a_1 = \frac{0.6}{(\varepsilon + IS_{1weno5})^2}$; $a_2 = \frac{0.3}{(\varepsilon + IS_{2weno5})^2}$;

$\omega_0 = \frac{a_0}{a_0 + a_1 + a_2}$; $\omega_1 = \frac{a_1}{a_0 + a_1 + a_2}$; $\omega_2 = \frac{a_2}{a_0 + a_1 + a_2}$;

Then compute the right flux given by a convex combination of the following parabolas

$\omega_{right} = \omega_0 \cdot (\frac{1}{3}n_{i-2} - \frac{7}{6}n_{i-1} + \frac{11}{6}n_i) + \omega_1 \cdot (-\frac{1}{6}n_{i-1} + \frac{5}{6}n_i + \frac{1}{3}n_{i+1}) + \omega_2 \cdot (\frac{1}{3}n_i + \frac{5}{6}n_{i+1} - \frac{1}{6}n_{i+2})$

At the left interface $x_{i-\frac{1}{2}}$, a similar formula is obtained using the following convex combination

$w_{left} = w_0 \cdot (-\frac{1}{6}n_{i-2} + \frac{5}{6}n_{i-1} + \frac{1}{3}n_i) + w_1 \cdot (\frac{1}{3}n_{i-1} + \frac{5}{6}n_i - \frac{1}{6}n_{i+1}) + w_2 \cdot (\frac{1}{3}n_{i+2} - \frac{7}{6}n_{i+1} + \frac{11}{6}n_i)$

where the optimal nonlinear weights are

$a_0 = \frac{0.3}{(\varepsilon + IS_{0weno5})^2}$; $a_1 = \frac{0.6}{(\varepsilon + IS_{1weno5})^2}$; $a_2 = \frac{0.1}{(\varepsilon + IS_{2weno5})^2}$

and the indicators of smoothness

$IS_{0weno5} = \frac{13}{12}(n_{i-2} - 2n_{i-1} + n_i)^2 + \frac{1}{4}(n_{i-2} - 4n_{i-1} + 3n_i)^2$

$IS_{1weno5} = \frac{13}{12}(n_{i-1} - 2n_i + n_{i+1})^2 + \frac{1}{4}(n_{i-1} - n_{i+1})^2$

$IS_{2weno5} = \frac{13}{12}(n_i - 2n_{i+1} + n_{i+2})^2 + \frac{1}{4}(3n_i - 4n_{i+1} + n_{i+2})^2.$

4.3.2. Weighted PowerENO Method

The last method that we use for our numerical simulations is Weighted PowerENO scheme [54]. This reconstruction have the same weighting strategy based on the smoothness indicators and the same algorithm such as WENO5 scheme. The new idea of this method is that it applies a class of limiters (powereno$_3$ or powermod$_3$ limiters based on the mean power$_3$ introduced above) computed at two neighboring second order differences in the classical third-order ENO reconstruction, improving in this way the resolution near discontinuities of the solution.

We use the power$_3$limiter of first and second order differences

$Power_3\left(x, y\right) = \min\left(x, y\right) \frac{x^2+y^2+2(\max(x,y))^2}{(x+y)^2}.$

Algorithm for the Weighted PowerENO method

We consider the following stencil points n_{i-2}, n_{i-1}, n_i, n_{i+1} and n_{i+2} in order to compute the lateral derivatives at $x_{i+\frac{1}{2}}$ and $x_{i-\frac{1}{2}}$.

For the next calculations we use the following notations:

$d_{i+\frac{1}{2}} = n_{i+1} - n_i$

$d_i = \frac{d_{i+\frac{1}{2}}+d_{i-\frac{1}{2}}}{2}$

$D_i = d_{i+\frac{1}{2}} - d_{i-\frac{1}{2}}$

Having these values, we compute

$P_{i-1/2} = \text{power}_3\text{eno}\ (D_{i-1}, D_i)$

$P_{i+1/2} = \text{power}_3\text{eno}\ (D_i, D_{i+1})$.

At the right interface $x_{i+\frac{1}{2}}$, compute the indicators of smoothness IS_0, IS_1 and IS_2 using the following expressions:

$IS_0 = \frac{13}{12}(P_{i-1/2})^2 + \frac{1}{4}(2n_i - 2n_{i-1} + P_{i-1/2})^2$

$IS_1 = \frac{13}{12}(n_{i-1} - 2n_i + n_{i+1})^2 + \frac{1}{4}(\frac{1}{2}(n_{i+1} - n_{i-1}))^2$

$IS_2 = \frac{13}{12}(P_{i+1/2})^2 + \frac{1}{4}(2(n_{i+1} - n_i) - P_{i+1/2})^2$.

Then, compute

$a_0 = \frac{0.2}{(10^{-6}+IS_0)^2}$; $a_1 = \frac{0.2}{(10^{-6}+IS_1)^2}$; $a_2 = \frac{0.6}{(10^{-6}+IS_2)^2}$;

$w_0 = \frac{a_0}{a_0+a_1+a_2}$; $w_1 = \frac{a_1}{a_0+a_1+a_2}$; $w_2 = \frac{a_2}{a_0+a_1+a_2}$;

Considering the expressions for the above parabolas, the convex combination at the right interface is:

$w_{right} = w_0 \cdot (n_i + \frac{1}{2}(n_i - n_{i-1}) + \frac{1}{3}P_{i-1/2}) + w_1 \cdot (n_i + \frac{1}{4}(n_{i+1} - n_{i-1}) + \frac{1}{12}(n_{i+1} -$

$2n_i + n_{i-1})) + w_2 \cdot (n_i + \frac{1}{2}(n_{i+1} - n_i) - \frac{1}{6}P_{i+1/2})$

At the left interface $x_{i-\frac{1}{2}}$, a similar formula is obtained using the following convex combination:

$w_{left} = w_0 \cdot (n_i - \frac{1}{2}(n_i - n_{i-1}) - \frac{1}{6}P_{i-1/2}) + w_1 \cdot (n_i - \frac{1}{4}(n_{i+1} - n_{i-1}) - \frac{1}{6}(n_{i+1} - 2n_i + n_{i-1})) + w_2 \cdot (n_i - \frac{1}{2}(n_{i+1} - n_i) + \frac{1}{3}P_{i+1/2})$

where the optimal weights are

$\omega_0 = \frac{a_0}{a_0+a_1+a_2}$; $\omega_1 = \frac{a_1}{a_0+a_1+a_2}$; $\omega_2 = \frac{a_2}{a_0+a_1+a_2}$

with the corresponding values of

$\alpha_0 = \frac{0.6}{(10^{-6}+IS_0)^2}$; $\alpha_1 = \frac{0.2}{(10^{-6}+IS_1)^2}$; $\alpha_2 = \frac{0.2}{(10^{-6}+IS_2)^2}$

and the smoothness indicators

$IS_0 = \frac{13}{12}(P_{i-1/2})^2 + \frac{1}{4}(2n_i - 2n_{i-1} + P_{i-1/2})^2$

$IS_1 = \frac{13}{12}(n_{i+1} - 2n_i + n_{i-1})^2 + \frac{1}{4}(\frac{1}{2}(n_{i+1} - n_{i-1}))^2$

$IS_2 = \frac{13}{12}(P_{i+1/2})^2 + \frac{1}{4}(2n_{i+1} - 2n_i - P_{i+1/2})^2$

where $P_{i-1/2}$ and $P_{i+1/2}$ are power$_3$eno limiters

$P_{i-1/2} = \text{power}_3\text{eno } (n_i - 2n_{i-1} + n_{i-2}, n_{i+1} - 2n_i + n_{i-1})$

$P_{i+1/2} = \text{power}_3\text{eno } (n_{i+1} - 2n_i + n_{i-1}, n_{i+2} - 2n_{i+1} + n_i).$

Chapter 5. Numerical Experiments

5.1 Introduction

Our general goal in this chapter consists of applying high order accurate shock capturing schemes, developed in Chapter 4, to approximate the solution of the nonlocal hyperbolic model proposed by Igoshin et al (2004) [22] and described in Chapter 3, with the purpose of coding a set of algorithms to perform numerical simulations for the better understanding of the mechanism of periodic pattern formation in myxobacteria colonies. The proposed algorithms will allow to describe how the myxobacteria cells can move on a line to the left or to the right and reverse their motion.

We show that in the absence of white noise sources introduced in the original model, the hyperbolic system of two coupled partial differential equations can reproduce the reversal process on a regular basis.

We construct the numerical solution using uniform grids for both spatial variable

x and the phase variable ϕ extended over their whole domains and assigning an approximate value of the solution on every point of the 2D grid at every time step. For the spatial fluxes (space and phase) we use as schemes upwind finite difference schemes with different order of accuracy, and Euler explicit algorithm to evolve in time.

The computation of the integral form of the fluxes for the internal clock variable is performed through the trapezoidal rule of numerical integration extended over the whole domain of the phase variable, using the approximated values of the solution at the grid points.

Explicit upwind schemes require a Courant-Friedrichs-Levy (CFL) restriction on the time step, Δt, in terms of the maximum wave speed and the spatial stepsizes Δx and $\Delta\phi$, of the form

$$\frac{\Delta t}{(\Delta x^2 + \Delta\phi^2)^{1/2}} \leq \frac{C}{1 + (1 + \epsilon)} \tag{5.1}$$

Here C is a positive constant such that $C < 1$ to ensure stability of the scheme. We use $C = 0.4$ in all our computations.

Since the first order scheme introduces more dissipation than needed, we have formulated high order accurate versions in space based on the third-order piecewise hyperbolic reconstruction procedures (PHM and PowerPHM) and fifth-order weighted essentially nonoscillatory reconstruction procedures (WENO5 and WPower$_3$WENO5) for the spatial variables. The third order Runge-Kutta method for the integration in time is the one proposed by Shu and Osher in [57] and allows the maximum time stepsize dictated by the first order upwind scheme (see Chapter 4).

5.2 Numerical Implementation

For simplicity, we start writing the equations of the myxobacteria model from Chapter 3 with $D_x = D_\phi = 0$, as:

$$\partial_t n + V(\phi)\partial_x n + \partial_\phi (W(x,\phi,t)n) = 0 \tag{5.2}$$

$$V(\phi) = \begin{cases} v, & 0 < \phi < \pi \\ -v, & -\pi < \phi < 0 \end{cases} \tag{5.3}$$

$$W(x,\phi,t) = \begin{cases} 1 + \epsilon\Omega(N_-(x,t)), & 0 < \phi < \pi \\ 1 + \epsilon\Omega(N_+(x,t)), & -\pi < \phi < 0 \end{cases} \tag{5.4}$$

Let us discretize the domain by choosing an uniform mesh (x_i, ϕ_j, t_m) by $x_i = ih$, $\phi_j = jh$, $t_m = mk$ with $h = \Delta x = \Delta\phi$ a space interval and $k = \Delta t$ a time step.

We define $x_{i+\frac{1}{2}} = x_i + \frac{h}{2} = (i+\frac{1}{2})h$ and $\phi_{j+\frac{1}{2}} = \phi_j + \frac{h}{2} = (j+\frac{1}{2})h$, the cell interfaces which separate the computational cells, and $\overline{n}_{i,j}^m \equiv \frac{1}{h^2}\int_{x_{i-\frac{1}{2}}}^{x_{i+\frac{1}{2}}}\int_{\phi_{j-\frac{1}{2}}}^{\phi_{j+\frac{1}{2}}} n(x,\phi,t_m)d\phi dx$ the cell average of $n(x,\phi,t)$ over the (i,j) computational cell $\left[x_{i-\frac{1}{2}}, x_{i+\frac{1}{2}}\right] \times \left[\phi_{j-\frac{1}{2}}, \phi_{j+\frac{1}{2}}\right]$.

As long as we are working with the space and phase variables, the numerical fluxes are reconstructed using a dimension-by-dimension procedure.

We want to find the numerical approximation of the function $n\left(x, \phi, t_m\right)$. By using the conservative discrete approximation of the spatial and phase derivatives, equation (5.2) takes the form

$$n_{i,j}^{m+1} = n_{i,j}^{m} - \frac{dt}{h}\left[V\left(\phi_j\right)\left(\tilde{n}_{i+\frac{1}{2},j} - \tilde{n}_{i-\frac{1}{2},j}\right)\right] - \frac{dt}{h}\left[\widetilde{W(x,\phi)}n|_{i,j+\frac{1}{2}} - \widetilde{W(x,\phi)}n|_{i,j-\frac{1}{2}}\right] \tag{5.5}$$

where $\tilde{n}_{i+\frac{1}{2},j}$, $\tilde{n}_{i-\frac{1}{2},j}$ $\widetilde{W(x,\phi)}n|_{i,j+\frac{1}{2}}$, and $\widetilde{W(x,\phi)}n|_{i,j-\frac{1}{2}}$are the interface fluxes.

5.2.1 Upwind Method

For the case of the upwind method of order one, where the interface fluxes are determined by the direction of wave propagation, we compute the interface fluxes in the following way: if the characteristic speed is positive, backward differences are used ($\tilde{n}_{i+\frac{1}{2},j} = \tilde{n}^{L}_{i+\frac{1}{2},j}$), otherwise forward differences are used ($\tilde{n}_{i+\frac{1}{2},j} = \tilde{n}^{R}_{i+\frac{1}{2},j}$).

For our problem, the first upwind procedure gives the following numerical fluxes:

- when $V(\phi_j) > 0$, we define

$$\begin{cases} \tilde{n}_{i+\frac{1}{2},j} = n_{i,j}^{m} \\ \tilde{n}_{i-\frac{1}{2},j} = n_{i-1,j}^{m} \end{cases} \tag{5.6}$$

- when $V(\phi_j) < 0$, we define

$$\begin{cases} \tilde{n}_{i+\frac{1}{2},j} = n^m_{i+1,j} \\ \tilde{n}_{i-\frac{1}{2},j} = n^m_{i,j} \end{cases} \tag{5.7}$$

- because the phase velocity is always positive, we have

$$\begin{cases} \widetilde{W(x,\phi)}n|_{i,j+\frac{1}{2}} = W(x_i,\phi_j)n^m_{i,j} \\ \widetilde{W(x,\phi)}n|_{i,j-\frac{1}{2}} = W(x_i,\phi_{j-1})n^m_{i,j-1} \end{cases} \tag{5.8}$$

5.2.2 Hyperbolic and Parabolic Reconstructions

For the numerical high accurate shock capturing schemes the most important step is the reconstruction. We look for the reconstruction of the function $n\left(x_i, \phi_j\right)$ up to the third and fifth order of accuracy.

First, from $n^m_{i,j}$, we reconstruct the point values of the function $n(x, \phi, t_m)$ via a suitable nonlinear piecewise polynomial interpolation $P_{i,j}(x, \phi)$, taking into account the conservation, accuracy and non-oscillatory requirements. For each cell we use this polynomial to reconstruct the values of the function at cell interface. For the reconstructions we use hyperbolic and parabolic procedures. As a result, at each cell interface the reconstruction produces two different values of the function $n(x, \phi, t_m)$ for each spatial direction.

Those values are:

$\tilde{n}^L_{i+\frac{1}{2},j} = P_{i,j}(x_{i+\frac{1}{2}}, \phi_j), \qquad \tilde{n}^R_{i+\frac{1}{2},j} = P_{i+1,j}(x_{i+\frac{1}{2}}, \phi_j)$

$$\tilde{n}^{L}_{i,j+\frac{1}{2}} = P_{i,j}(x_i, \phi_{j+\frac{1}{2}}), \qquad \tilde{n}^{R}_{i,j+\frac{1}{2}} = P_{i,j+1}(x_i, \phi_{j+\frac{1}{2}})$$

The hyperbolic and parabolic procedures give the following numerical fluxes:

- when $V(\phi_j) > 0$, we define

$$\tilde{n}_{i+\frac{1}{2},j} = P_{i,j}\left(x_{i+\frac{1}{2}}, \phi_j\right) \tag{5.9}$$

- when $V(\phi_j) < 0$, we define

$$\tilde{n}_{i+\frac{1}{2},j} = P_{i+1,j}\left(x_{i+\frac{1}{2}}, \phi_j\right) \tag{5.10}$$

- when $(W(x,\phi,t) > 0)$, we define

$$\widetilde{W(x,\phi)}n|_{i,j+\frac{1}{2}} = P_{i,j}W(x_i, \phi_{j+\frac{1}{2}}) \tag{5.11}$$

With these reconstructed values of hyperbolas (for the PHM methods) or parabolas (for the WENO5 methods), we can approximate the fluxes $\tilde{n}_{i+\frac{1}{2},j}$, $\widetilde{W(x,\phi)}n|_{i,j+\frac{1}{2}}$. Analogous, we can approximate the fluxes $\tilde{n}_{i-\frac{1}{2},j}$, $\widetilde{W(x,\phi)}n|_{i,j-\frac{1}{2}}$.

5.3 Numerical Solutions

We consider our hyperbolic problem with the initial condition a piecewise constant signal, periodic in x and ϕ for each of the areas where the dynamics is directly reverse or refractory.

We start with the function $n(x, \phi, t = 0) = 1 + 0.1 \sin(x) \sin(\phi)$ on the interval $[-\pi, \pi] \times [-\pi, \pi]$. We use a grid of 100×100 points with a CFL number of 0.4 and the time long enough to obtain one complete period. For the first experiments we analyze the increasing of ϵ. We compute the approximate solution for upwind, PHM, WENO5 and WPower$_3$ENO5 using $\alpha = \pi/10$ and $r = 4$. The total density of bacteria at point x and time t is $N_+(x, t) + N_-(x, t)$.

When $\epsilon = 0$ the system of conservation laws (5.2)-(5.4) transforms in a system of linear wave equations and as we can see, the numerical solution can be approximated using upwind schemes of any order of accuracy in space. We observe, in Fig. 5.1, that a numerical dissipation is introduced by the upwind method compared with PHM, WENO5 and WPower$_3$ENO5. By increasing the nonlinearity (the value of ϵ), reversals of bacteria occur earlier and a numerical dissipation appear even if we use high order numerical schemes. This is explained by the presence of the nonlocal nonlinearities of the fluxes which produce an analytic dissipation mechanism.

The density of time-reversal points (reversal point density) is represented as

$$RPD = n_{LR} + n_{RL} = n(x, \phi = 0+, t) + n(x, \phi = -\pi+, t) \tag{5.12}$$

In Fig. 5.5 and Fig. 5.6 we show the plots of the RPD for the PHM scheme and for PowerPHM scheme with $\alpha = \pi/10$ and $r = 4$, as nonlinearity increases.

As we can see from the Fig. 5.5 (a), (b) and Fig. 5.6 (a), (b) a slight decrease of

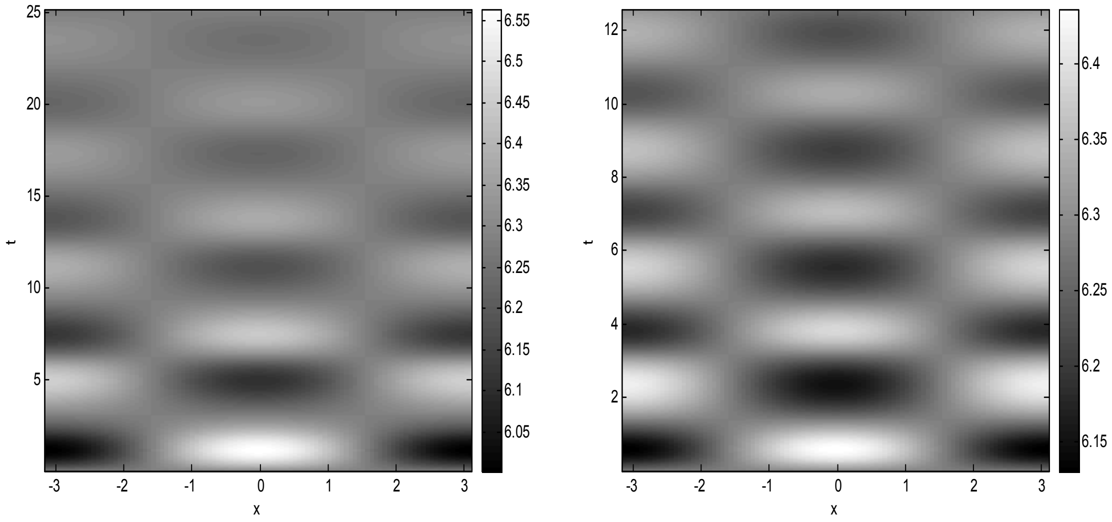

(a) $\epsilon = 0$

(b) $\epsilon = 1.2$

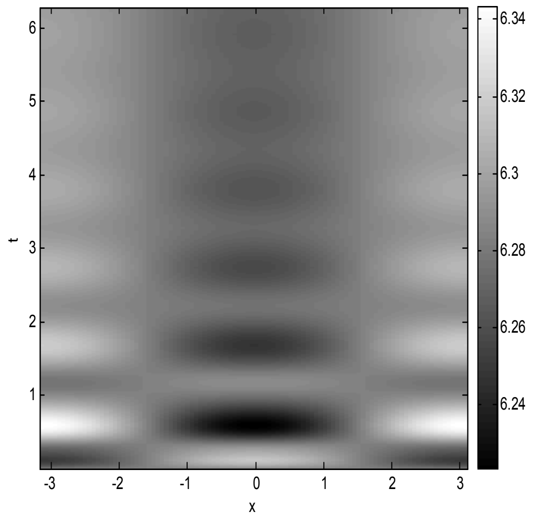

(c) $\epsilon = 12$

Fig 5.1: Grey scale plots of the total density $N_+(x,t) + N_-(x,t)$ for $\alpha = \pi/10$, $r = 4$, and (a) $\epsilon = 0$, (b) $\epsilon = 1.2$, (c) $\epsilon = 12$ with the upwind method.

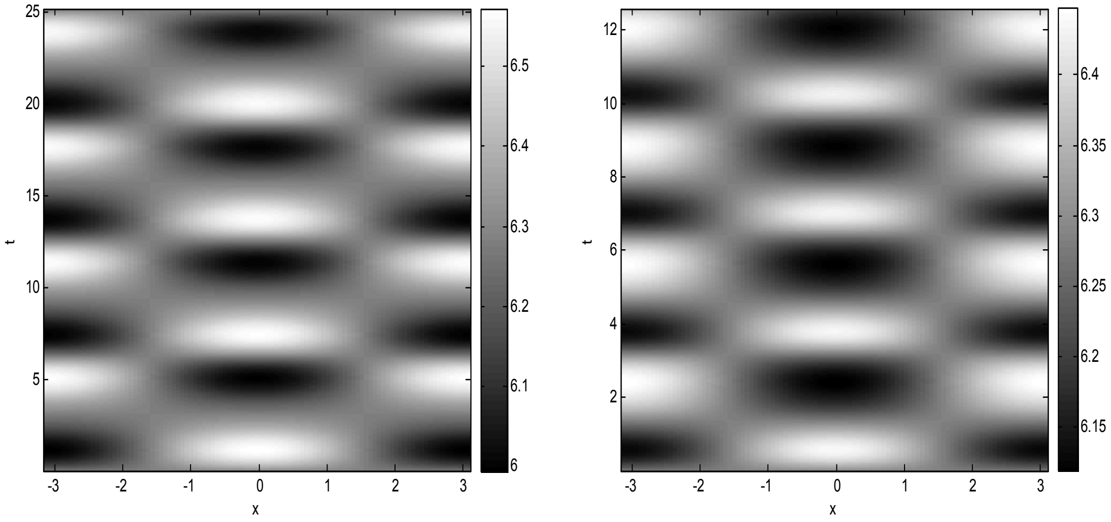

(a) $\epsilon = 0$ (b) $\epsilon = 1.2$

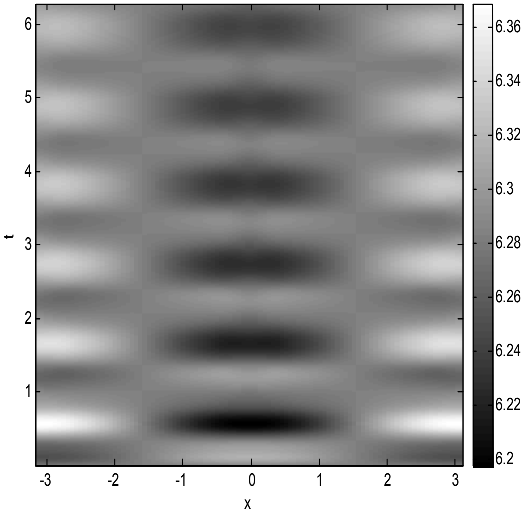

(c) $\epsilon = 12$

Fig 5.2: Grey scale plots of the total density $N_+(x,t) + N_-(x,t)$ for $\alpha = \pi/10$, $r = 4$, and (a) $\epsilon = 0$, (b) $\epsilon = 1.2$, (c) $\epsilon = 12$ with the PHM method.

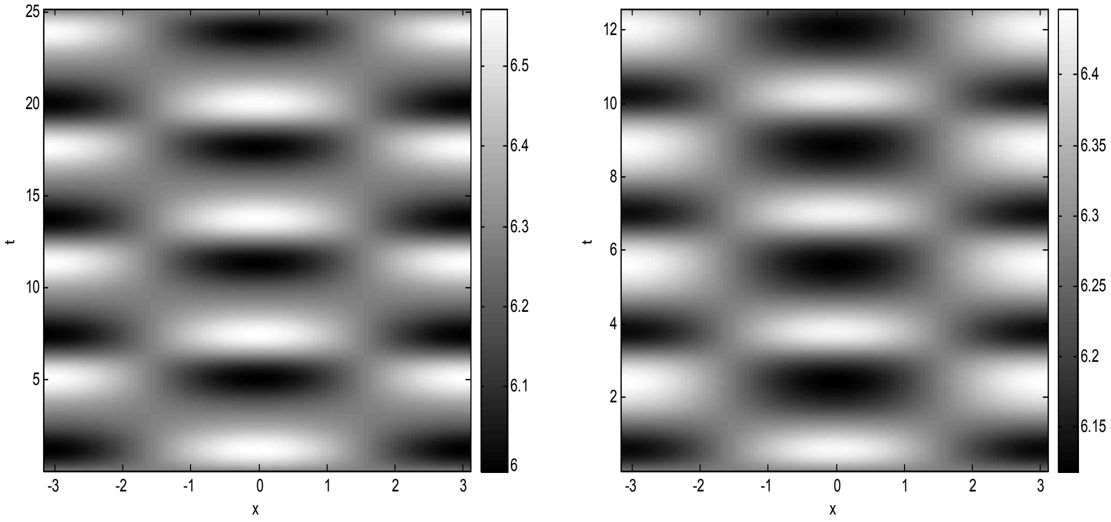

(a) $\epsilon = 0$

(b) $\epsilon = 1.2$

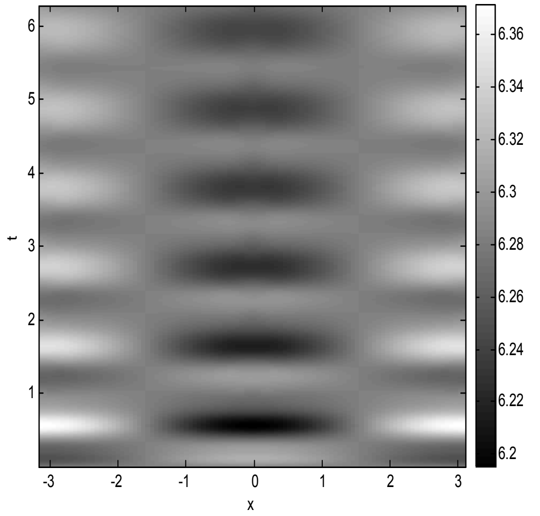

(c) $\epsilon = 12$

Fig 5.3: Grey scale plots of the total density $N_+(x,t) + N_-(x,t)$ for $\alpha = \pi/10$, $r = 4$, and (a) $\epsilon = 0$, (b) $\epsilon = 1.2$, (c) $\epsilon = 12$ with the WENO5 method.

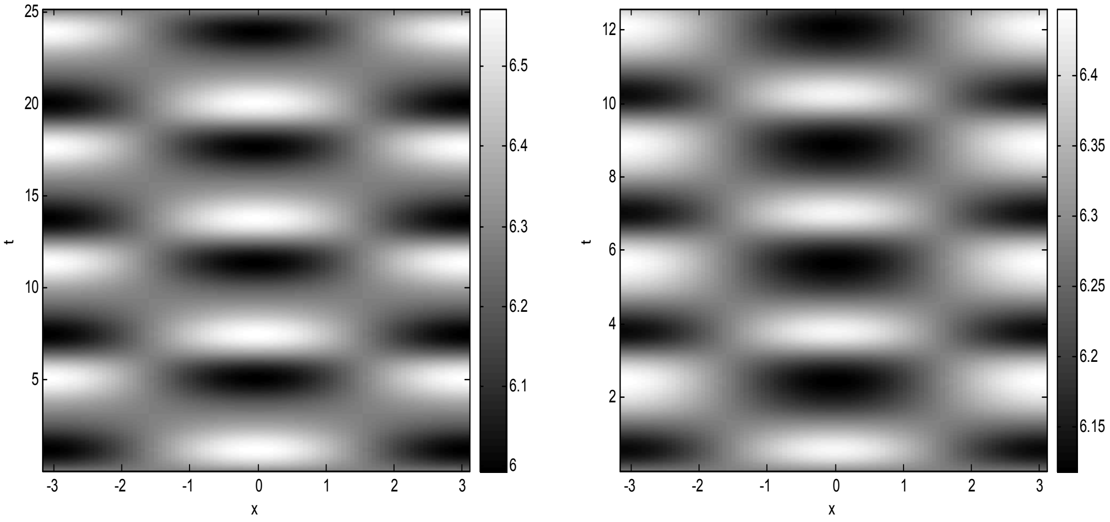

(a) $\epsilon = 0$ (b) $\epsilon = 1.2$

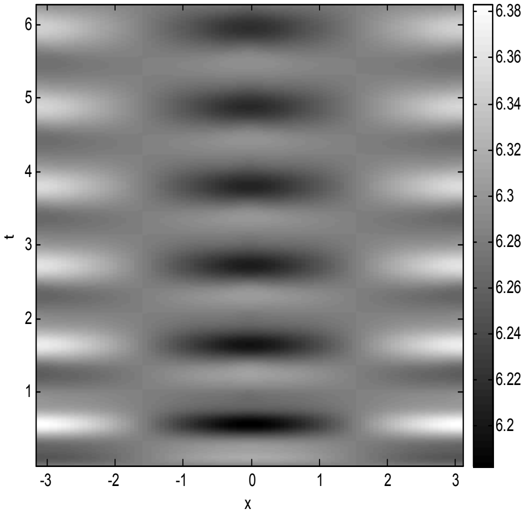

(c) $\epsilon = 12$

Fig 5.4: Grey scale plots of the total density $N_+(x,t) + N_-(x,t)$ for $\alpha = \pi/10$, $r = 4$, and (a) $\epsilon = 0$, (b) $\epsilon = 1.2$, (c) $\epsilon = 12$ with the WPower$_3$ENO5 method.

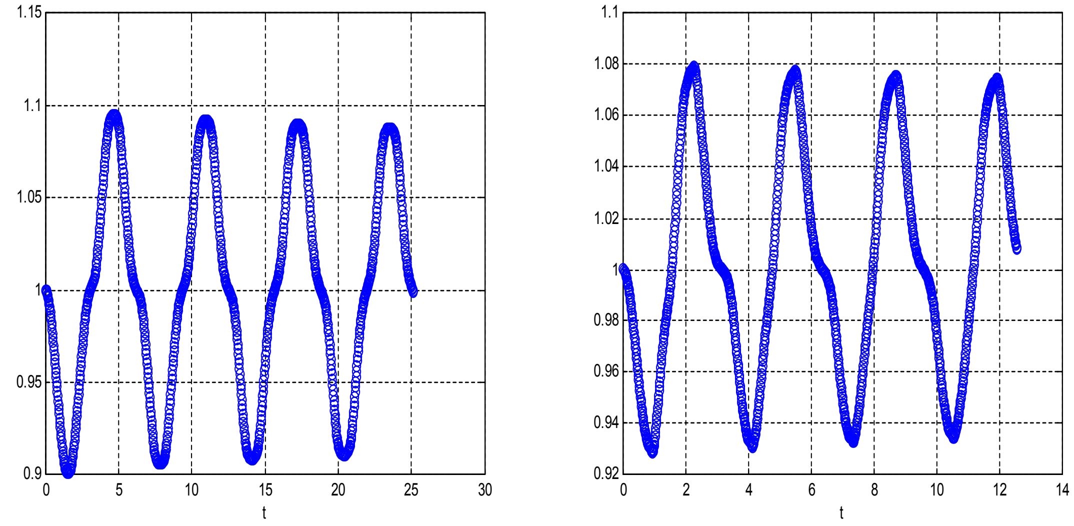

(a) $\epsilon = 0$

(b) $\epsilon = 1.2$

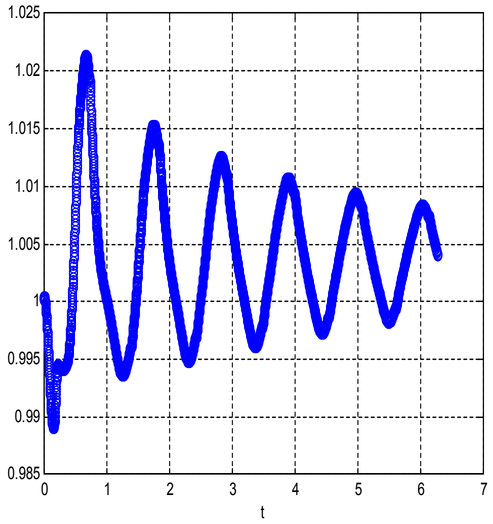

(c) $\epsilon = 12$

Fig 5.5: Plots of the RPD *vs* time for $\alpha = \pi/10$, $r = 4$ and (a) $\epsilon = 0$, (b) $\epsilon = 1.2$, (c) $\epsilon = 12$ with the PHM method.

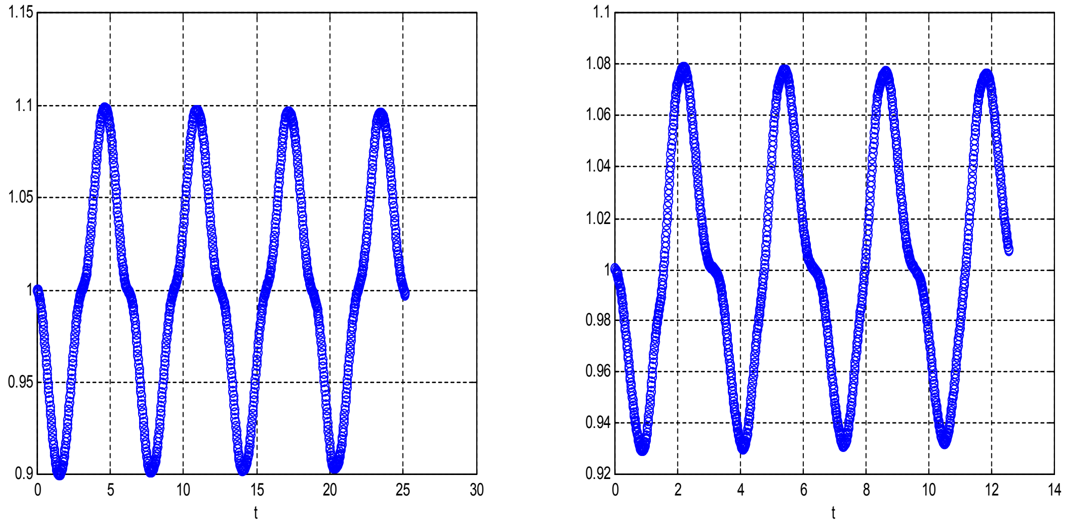

(a) $\epsilon = 0$

(b) $\epsilon = 1.2$

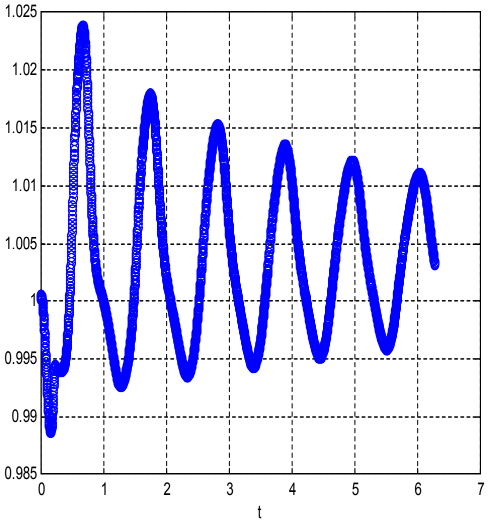

(c) $\epsilon = 12$

Fig 5.6: Plots of the RPD *vs* time for $\alpha = \pi/10$, $r = 4$ and (a) $\epsilon = 0$, (b) $\epsilon = 1.2$, (c) $\epsilon = 12$ with the PowerPHM method.

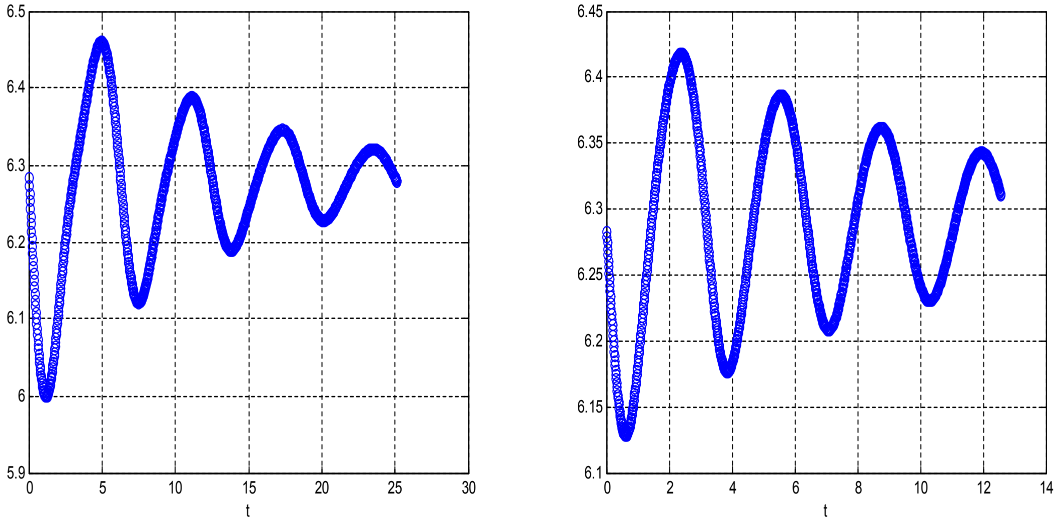

(a) $\epsilon = 0$

(b) $\epsilon = 1.2$

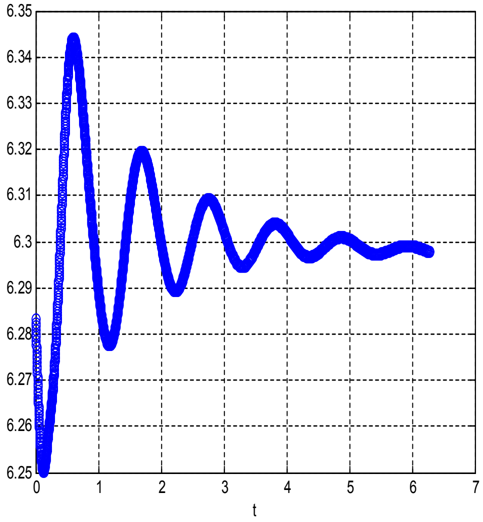

(c) $\epsilon = 12$

Fig 5.7: Plots of the total density *vs* time for $\alpha = \pi/10$, $r = 4$ and (a) $\epsilon = 0$, (b) $\epsilon = 1.2$, (c) $\epsilon = 12$ with the upwind method.

the maxima of the reversal point density is noticed due to numerical errors in case of PHM method in comparison with the PowerPHM method. Also, from the Fig. 5.5 (c) and Fig. 5.6 (c), the evolution of the RPD towards a constant value is slow.

Next, we display the total density for $\alpha = \pi/10$, $r = 4$ with upwind method.

Using the method of first order of accuracy in space, the plots of the total density (Fig. 5.7) show a strong dissipation due to numerical noise and finally, the patterns disappear and converge to uniform stationary state, as shown in Fig. 5.7 (c).

Using these numerical approximations for the case when the signaling is strong, we are able to analyze the parameters of the model to locate Hopf bifurcations. When using the first-order numerical method the behavior is the following: the diffusion is present and the system tends to spread the Hopf bifurcations to states that are not interesting from a biological standpoint. In the case of non-signaling state ($\epsilon = 0$), the analytical solution is perfectly recovered and for the ultrastrong signaling ($\epsilon = 12$), the rippling phenomenon doesn't exist and the system goes to a stationary state.

For the second experiment we consider the case of a very large exponent of r ($r = 20$). This is equivalent with a generic saturating function with a jump, instead of the logistic one ($r = 4$).

In the following figures we show the plots of total density and reversal point density for $r = 20$.

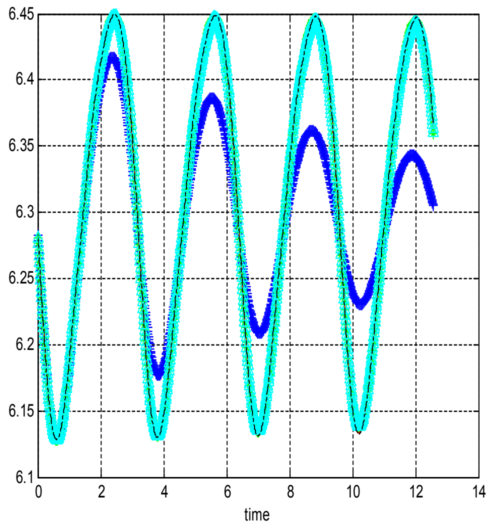

Fig 5.8: Plots of the total density *vs* time with $r = 20$. Comparisons between upwind ('b+'), WENO5 ('c^') and WPower$_3$ENO5 ('k-.').

By increasing the parameter r in the function $\Omega(N)$, there are no modifications for the patterns, the amplitude of the traveling waves has the same shape like in the case when we use $r = 4$.

The other analysis consists of changing the parameter α. The numerical results of the reversal point density are displayed in Fig. 5.10, where we use the WENO5 method for the simulations.

We can observe that as α decreases, the frequency of the traveling waves increases.

For the next numerical simulation we consider the following initial condition

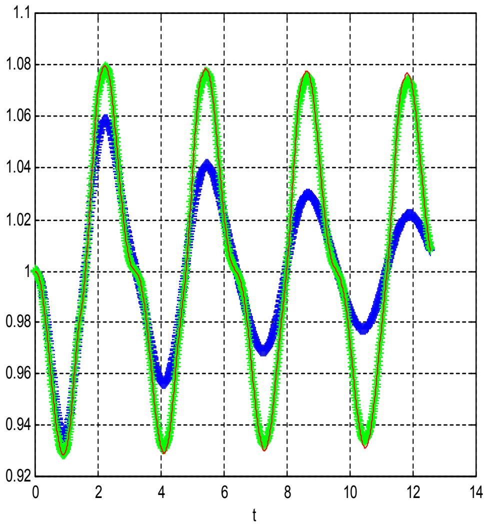

Fig 5.9: Plots of the reversal point density *vs* time with $r = 20$. Comparisons between upwind ('b+'), PHM ('g*'), Power$_3$PHM ('r-').

$n(x, \phi, t = 0) = 1 + 0.1 \sin(kx) \sin(\phi)$ with a fixed $\alpha = \pi/5$.

In Figure 5.11, we show the surface plots of the reversal point density with $k = 2$, $k = 4$, and $k = 6$.

As we can see from the simulations, when $k = 2$ the periodic patterns are present. Fig. 5.11 (b) shows a transient stage to the stationary solution (the case when $k = 6$).

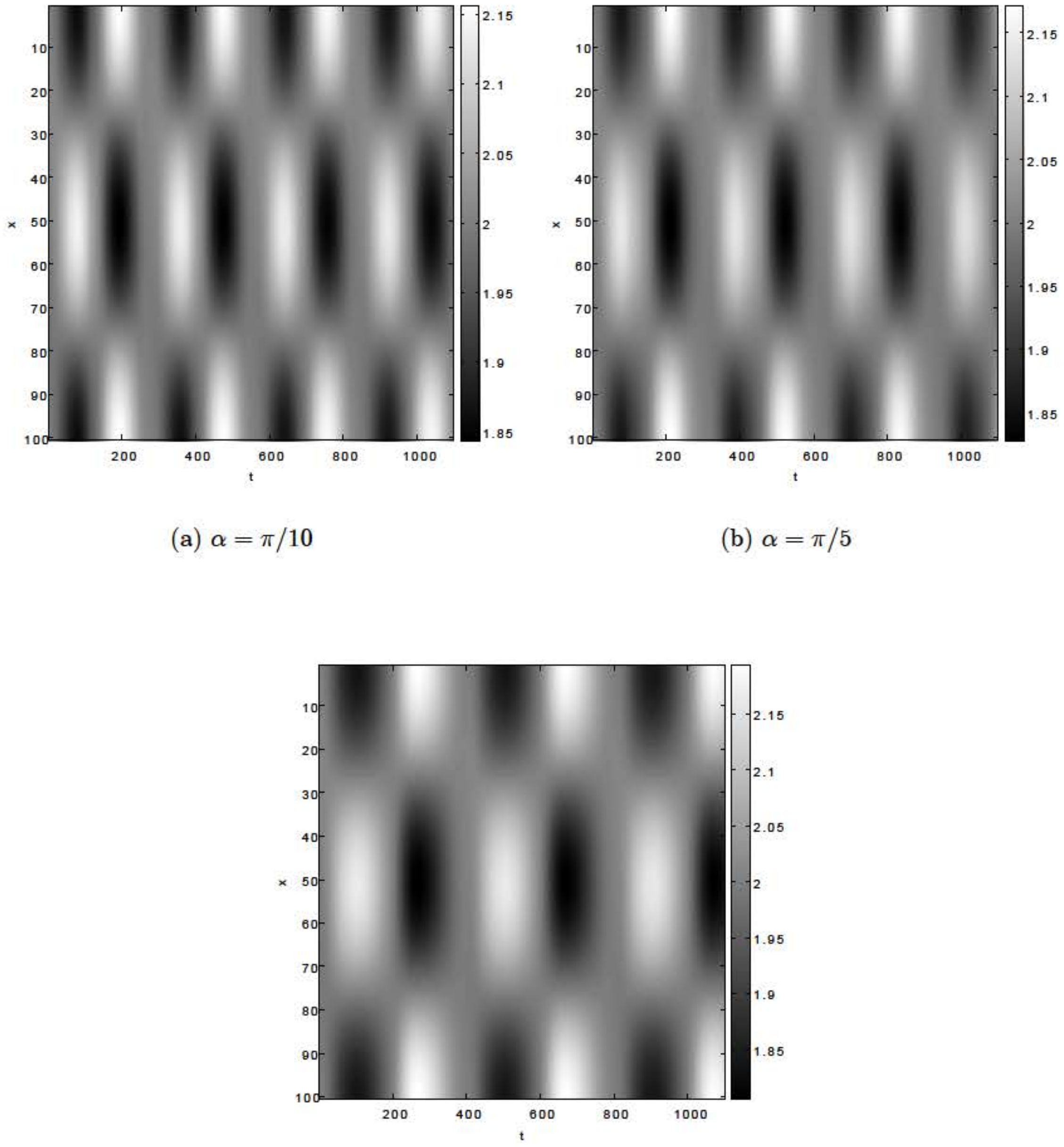

(a) $\alpha = \pi/10$

(b) $\alpha = \pi/5$

(c) $\alpha = \pi/2$

Fig 5.10: Grey scale plots of the RPD for $r = 4$, $\epsilon = 1.2$, time $= 4\pi$ and (a) $\alpha = \pi/10$, (b) $\alpha = \pi/5$, (c) $\alpha = \pi/2$.

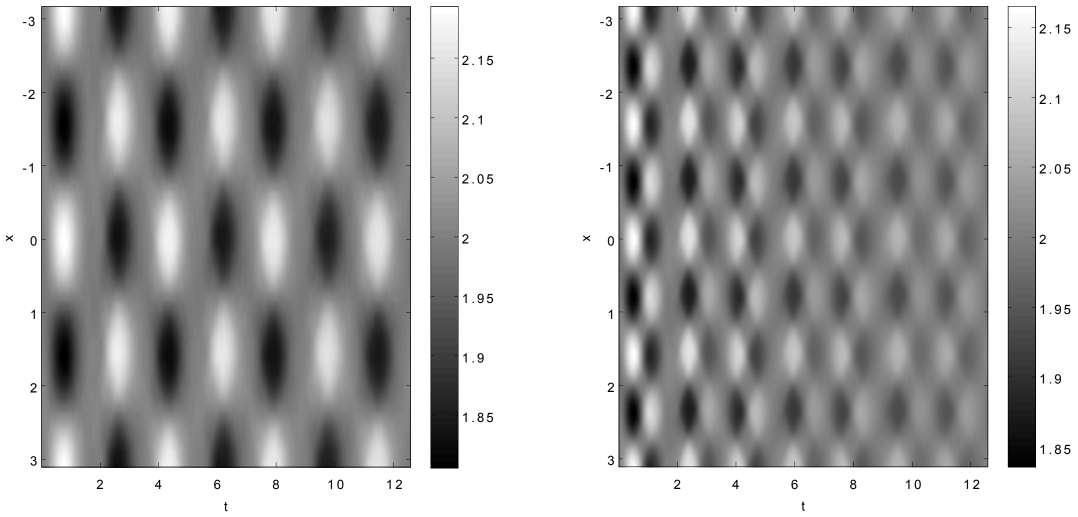

(a) $k = 2$ (b) $k = 4$

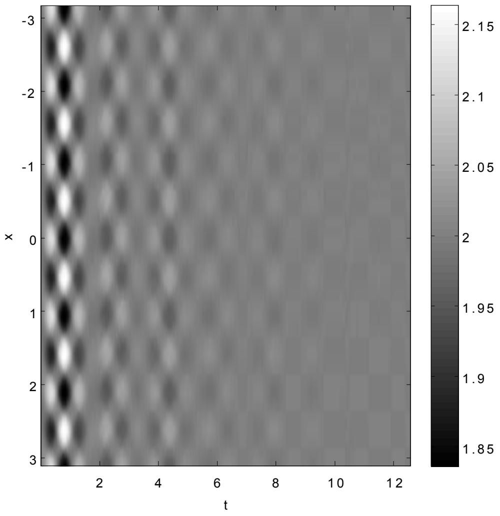

(c) $k = 6$

Fig 5.11: Contour plots of the RPD for $r = 4$, $\epsilon = 1.2$, time $= 4\pi$, $\alpha = \pi/5$ and wavenumber: (a) $k = 2$, (b) $k = 4$, (c) $k = 6$. The simulations were realized with PHM method.

Chapter 6. Wavelength Selection of Rippling Patterns in Myxobacteria

6.1 Introduction

In this chapter, we consider Igoshin et al's continuum one-dimensional (1D) model for rippling [21,22] described in Chapter 3, solve it numerically and interpret the results by a study of the small nonlinearity limit. An extension of this model to 2D can be found in [23] and related agent-based models in [72]. Previous work has shown that numerical solutions of the continuum model exhibit rippling [22]. Surprisingly, the analysis of the small nonlinearity limit does not provide a selection rule for the observed wavelength of ripples [22]. In contrast with these results, we show that the small nonlinearity limit does provide a description of the rippling instability and it supplies the critical wavenumber of the periodic patterns in terms of the refractory period. In fact, careful consideration of flux continuity at the different stages of one cycle of the internal clock of myxobacteria shows that the limiting equation for the cell density is of Fokker-Planck type but it contains an additional source term. The extra source term is the cell density times a nonlocal growth rate that vanishes as the refractory period tends to zero. The source term is key new element in our analysis, as it produces dissipation even in the absence of diffusion. Thus the role of the source term is similar to that of collision terms in the Boltzmann transport equation. The balance between advection in space and time and dissipation due to the "collision term" selects the wavelength of the rippling patterns that issue forth from the uniform stationary state. These patterns are periodic in time and space. Numerical solutions of the full model equations show that the pattern frequency decreases as the strength of the nonlinearity increases.

It is interesting to contrast the behavior of the present myxobacteria model with the well-known synchronization of globally coupled phase oscillators described by the Kuramoto model [1, 35]. The Kuramoto oscillators move on a circle with their own random natural frequency and their mutual interaction through a mean field tends to synchronize them. Partial or complete synchronization is achieved for sufficiently strong coupling through a nonequilibrium phase transition. Igoshin et al's model describes phase oscillators with an internal clock whose angular speed changes according to their interaction with oppositely moving oscillators. Since the Igoshin oscillators move with a constant positive or negative velocity, patterns arising from appropriate initial conditions persist in the absence of interaction. In this case, mean-field interaction among oscillators may produce loss of rhythmicity resulting in the destruction of patterns. This change appears as a nonequilibrium phase transition at critical values of parameters that has been explicitly shown in the weak coupling limit.

The rest of the chapter is as follows. The weakly nonlinear limit is examined in Section 6.2, where the limiting Fokker-Planck type equation with source term is derived. The linear stability of its uniform stationary solution is analyzed in Section 6.3. In the absence of diffusion and for disturbances with frequency one (same as that of the signaling solution without nonlinear terms), we find that rippling patterns appear for disturbances with wavenumber less than one, whatever the refractory period. Increasing the wavenumber k may result in the cancellation of patterns, as the uniform stationary solution becomes linearly stable. Since diffusion has a stabilizing role for the uniform solution (producing a negative term proportional to k^2 in the real part of eigenvalues), unavoidable numerical noise should tend to annihilate the periodic patterns and be more effective as k increases. Section 6.4 contains the results of numerical solutions of the full model equations. The findings of the linear stability analysis and the wavenumber selection criteria are confirmed. In addition, we observe a rich variety of stable periodic patterns comprising standing and traveling waves as numerical solutions of the model equations for moderate and strong signaling between cells. Section 6.5 contrasts our findings with the behavior of the Kuramoto model for the synchronization of phase oscillators. The last section contains our conclusions.

6.2 Weak Signaling Limit

For $\epsilon = 0$, (3.12) becomes

$$\partial_t n + \operatorname{sign}(\phi)\partial_x n + \partial_\phi n = 0, \tag{6.1}$$

whose solution is [22]

$$n = \begin{cases} f(x-\phi, t-\phi), & 0 < \phi < \pi, \\ f(x+\phi, t-\phi), & -\pi < \phi < 0. \end{cases} \tag{6.2}$$

Here $f(x,t)$ is an arbitrary function, 2π-periodic in its second argument. $f(x,t)$ and $f(x-\pi, t+\pi)$ represent the densities of left-to-right and of right-to-left reversals, respectively. Then, according to (3.7), $n_{\mathrm{RPD}}(x,t) = f(x,t) + f(x-\pi, t+\pi)$ is the reversal point density (RPD) in the weakly nonlinear limit and weak diffusion limit as $\epsilon \to 0+$. This limit is also called the *weak signaling limit* [22]. In (6.2), $n(x,t,\phi)$ is continuous and 2π-periodic in ϕ. The constant solution, $f = \hat{N}/(2\pi)$, is a particular solution of (3.12).

Igoshin et al have derived a Fokker-Planck equation for f in the weakly nonlinear limit as $\epsilon \to 0$ by using physical arguments and also by singular perturbation methods (see Appendix in [22]). Their derivation missed the collision-type source term that we find in this chapter. Finding this term requires delving more deeply in the perturbation method, therefore we describe this method from scratch. In the limit as

$\epsilon \to 0$, we seek a solution

$$n = n_0(x,t,\phi,\tau) + \epsilon\, n_1(x,t,\phi,\tau) + O(\epsilon^2), \quad \tau = \frac{\epsilon t}{2\pi}, \tag{6.3}$$

$$n_0(x,t,\phi,\tau) = \begin{cases} f(x-\phi, t-\phi, \tau), & 0 < \phi < \pi, \\ f(x+\phi, t-\phi, \tau), & -\pi < \phi < 0, \end{cases} \tag{6.4}$$

so that n_1 is 2π-periodic in ϕ. Note that the function f in (6.4) has the form (6.2) with an additional dependence upon the slow time τ. The equation for n_1 is

$$[\partial_t + \mathrm{sign}(\phi)\partial_x + \partial_\phi]n_1 = \left(\mathcal{D}_x\partial_x^2 + \mathcal{D}_\phi\partial_\phi^2 - 2\pi\Omega_-\chi_{[\alpha,\pi]}\partial_\phi - 2\pi\Omega_+\chi_{[-\pi+\alpha,0]}\partial_\phi - \partial_\tau\right)\frac{n_0}{2\pi}, \tag{6.5}$$

with

$$\begin{aligned} N_+(x,t,\tau) &= \int_0^\pi f(x-\psi, t-\psi, \tau)\, d\psi, \\ N_-(x,t,\tau) &= \int_{-\pi}^0 f(x+\psi, t-\psi, \tau)\, d\psi = \int_0^\pi f(x-\psi, t+\psi, \tau)\, d\psi, \\ \Omega_\pm(x,t,\tau) &= \Omega(N_\pm(x,t,\tau)), \quad N_\pm(x,t,\tau) = \int_0^\pi f(x-\psi, t\mp\psi, \tau)\, d\psi. \end{aligned} \tag{6.6}$$

Continuity of the flux $J = \{1+\epsilon\Omega_-\chi_{[\alpha,\pi]} + \epsilon\Omega_+\chi_{[-\pi+\alpha,0]}\}n - \mathcal{D}_\phi\partial_\phi n/(2\pi)$, across angle boundaries and (6.3) yield

$$[n_1]_{\phi=0} \equiv n_1|_{\phi=0+} - n_1|_{\phi=0-} = \Omega_+ n_0|_{\phi=0-} + \frac{\mathcal{D}_\phi}{2\pi}[\partial_\phi n_0]|_{\phi=0}, \tag{6.7}$$

$$[n_1]_{\phi=\alpha} \equiv n_1|_{\phi=\alpha+} - n_1|_{\phi=\alpha-} = -\Omega_- n_0|_{\phi=\alpha+} + \frac{\mathcal{D}_\phi}{2\pi}[\partial_\phi n_0]|_{\phi=\alpha}, \tag{6.8}$$

$$[n_1]_{\phi=-\pi+\alpha} \equiv n_1|_{\phi=-\pi+\alpha+} - n_1|_{\phi=-\pi+\alpha-} = -\Omega_+ n_0|_{\phi=-\pi+\alpha+} + \frac{\mathcal{D}_\phi}{2\pi}[\partial_\phi n_0]|_{\phi=-\pi+\alpha}, \tag{6.9}$$

$$[n_1]_{\phi=\pi} \equiv n_1|_{\phi=-\pi+} - n_1|_{\phi=\pi-} = \Omega_- n_0|_{\phi=\pi-} + \frac{\mathcal{D}_\phi}{2\pi}[\partial_\phi n_0]|_{\phi=\pi}. \tag{6.10}$$

From (6.4) and (6.5), we obtain along the characteristics

$$x(\phi) = x_0 + \mathrm{sign}(\phi)\phi, \quad t(\phi) = t_0 + \phi, \quad f(\phi) = f(x_0, t_0), \tag{6.11}$$

the following equation for n_1:

$$\frac{dn_1}{d\phi} = \begin{cases} \{L_+ + \chi_{[\alpha,\pi]}(\partial_{x_0} + \partial_{t_0})\Omega_-(x_0 + \phi, t_0 + \phi)\}f, & 0 < \phi < \pi, \\ \{L_- - \chi_{[\alpha-\pi,0]}(\partial_{x_0} - \partial_{t_0})\Omega_+(x_0 - \phi, t_0 + \phi)\}f, & -\pi < \phi < 0. \end{cases} \tag{6.12}$$

In (6.12) we have defined

$$L_\pm = \frac{1}{2\pi}[\mathcal{D}_x \partial_{x_0}^2 + \mathcal{D}_\phi(\partial_{x_0} \pm \partial_{t_0})^2 - \partial_\tau]. \tag{6.13}$$

Ignoring the initial condition for n_1, the solution of (6.12) along the characteristics (6.11) is

$$n_1^p = \begin{cases} \phi L_+ f + \left(1 - \frac{\alpha}{\pi}\right) \Omega_-(x_0 + \alpha, t_0 + \alpha, \tau)\, f, & 0 < \phi < \alpha \\ \phi L_+ f + (\partial_{x_0} + \partial_{t_0}) f \int_\alpha^\phi \Omega_- d\phi + C_\alpha, & \alpha < \phi < \pi, \\ \phi L_- f + (\partial_{x_0} - \partial_{t_0}) f \int_\phi^0 \Omega_+ d\phi + C_0, & \alpha - \pi < \phi < 0, \\ \phi L_- f + C_{\alpha-\pi}, & -\pi < \phi < \alpha - \pi, \end{cases} \tag{6.14}$$

where $f = f(x_0, t_0, \tau)$, the constants of integration C_j are independent of ϕ, and

$$\begin{cases} \int_\alpha^\phi \Omega_- d\phi = \int_\alpha^\phi \Omega\left(\int_0^\pi f(x_0 + \phi' - \psi, t_0 + \phi' + \psi, \tau) d\psi\right) d\phi', \\ \int_\phi^0 \Omega_+ d\phi = \int_\phi^0 \Omega\left(\int_0^\pi f(x_0 - \phi' - \psi, t_0 + \phi' - \psi, \tau) d\psi\right) d\phi'. \end{cases} \tag{6.15}$$

To determine the constants C_j in (6.14), we impose the jump conditions (6.7)-(6.9). Using (6.4), $[\partial_\phi n_0]|_{\phi=\alpha} = [\partial_\phi n_0]|_{\phi=-\pi+\alpha} = 0$, $[\partial_\phi n_0]|_{\phi=\pi} = 2\partial_x f(x_0 - \pi, t_0 + \pi, \tau)$,

$[\partial_\phi n_0]|_{\phi=0} = -2\partial_x f(x_0, t_0, \tau)$, and we find

$$
\begin{aligned}
C_\alpha &= -\frac{\alpha}{\pi}\,\Omega_-(x_0+\alpha, t_0+\alpha, \tau)\, f(x_0, t_0, \tau), && (6.16)\\
C_0 &= \left[\Big(1-\frac{\alpha}{\pi}\Big)\Omega_-(x_0+\alpha, t_0+\alpha, \tau) - \Omega_+(x_0, t_0)\right] f(x_0, t_0, \tau) + \frac{\mathcal{D}_\phi}{\pi}\partial_x f(x_0, t_0, \tau), && \\
& && (6.17)
\end{aligned}
$$

$$
\begin{aligned}
C_{\alpha-\pi} = &\left[\Omega_+(x_0-\alpha+\pi, t_0+\alpha-\pi, \tau) + \Big(1-\frac{\alpha}{\pi}\Big)\Omega_-(x_0+\alpha, t_0+\alpha, \tau) - \Omega_+(x_0, t_0)\right]\\
&\times f(x_0, t_0, \tau) + (\partial_{x_0} - \partial_{t_0})\left(f(x_0, t_0, \tau)\int_{\alpha-\pi}^{0}\Omega_+ d\phi\right) + \frac{\mathcal{D}_\phi}{\pi}\partial_x f(x_0, t_0, \tau). \quad (6.18)
\end{aligned}
$$

The integral on the right hand side of (6.18) can be rewritten as

$$
\begin{aligned}
\int_{\alpha-\pi}^{0}\Omega_+ d\phi &= \int_{\alpha-\pi}^{0}\Omega\left(\int_0^\pi f(x_0-\phi-\psi, t_0+\phi-\psi, \tau)d\psi\right)d\phi\\
&= \int_{\alpha}^{\pi}\Omega\left(\int_0^\pi f(x_0+\pi-\phi-\psi, t_0-\pi+\phi-\psi, \tau)d\psi\right)d\phi\\
&= \int_{\alpha}^{\pi}\Omega\left(\int_0^\pi f(x_0+\pi-\phi-\psi, t_0+\pi+\phi-\psi, \tau)d\psi\right)d\phi\\
&= \int_{\alpha}^{\pi}\Omega\left(\int_0^\pi f(x_0-\phi+\psi, t_0+\phi+\psi, \tau)d\psi\right)d\phi. \qquad (6.19)
\end{aligned}
$$

We have used that $f(x, t, \tau)$ is 2π-periodic in t and the change of variable $\pi - \psi \to \psi$ to simplify the integral in (6.19). The first term in $C_{\alpha-\pi}$ can be similarly simplified, thereby producing

$$
\begin{aligned}
C_{\alpha-\pi} = &\left[\Omega\left(\int_0^\pi f(x_0-\alpha+\psi, t_0+\alpha+\psi, \tau)d\psi\right) - \Omega\left(\int_0^\pi f(x_0-\psi, t_0-\psi, \tau)d\psi\right)\right.\\
&\left.+\Big(1-\frac{\alpha}{\pi}\Big)\Omega\left(\int_0^\pi f(x_0+\alpha-\psi, t_0+\alpha+\psi, \tau)d\psi\right)\right] f\\
&+ (\partial_{x_0} - \partial_{t_0})\left[f\int_\alpha^\pi \Omega\left(\int_0^\pi f(x_0-\phi+\psi, t_0+\phi+\psi, \tau)d\psi\right)d\phi\right] + \frac{\mathcal{D}_\phi}{\pi}\partial_x f.\\
& \qquad (6.20)
\end{aligned}
$$

The condition (6.10) ensuring 2π-periodicity in ϕ provides the sought equation for f:

$$\begin{aligned}
&\partial_\tau f + \partial_x(Uf) + \partial_t(Vf) - (\mathcal{D}_x + \mathcal{D}_\phi)\partial_x^2 f - \mathcal{D}_\phi \partial_t^2 f = f\,Q[f] \\
&\quad - \frac{\mathcal{D}_\phi}{\pi}\partial_x[f(x,t,\tau) - f(x-\pi, t+\pi, \tau)], \qquad (6.21) \\
&U = \int_\alpha^\pi \left[\Omega\left(\int_0^\pi f(x-\phi+\psi, t+\phi+\psi, \tau)d\psi\right)\right. \\
&\quad \left. - \,\Omega\left(\int_0^\pi f(x+\phi-\psi, t+\phi+\psi, \tau)d\psi\right)\right] d\phi, \qquad (6.22) \\
&V = -\int_\alpha^\pi \left[\Omega\left(\int_0^\pi f(x-\phi+\psi, t+\phi+\psi, \tau)d\psi\right)\right. \\
&\quad \left. + \,\Omega\left(\int_0^\pi f(x+\phi-\psi, t+\phi+\psi, \tau)d\psi\right)\right] d\phi, \qquad (6.23)
\end{aligned}$$

$$\begin{aligned}
Q[f] = {} & \Omega\left(\int_0^\pi f(x+\psi, t-\psi, \tau)d\psi\right) + \Omega\left(\int_0^\pi f(x-\psi, t-\psi, \tau)d\psi\right) \\
& - \Omega\left(\int_0^\pi f(x+\alpha-\psi, t+\alpha+\psi, \tau)d\psi\right) \\
& - \Omega\left(\int_0^\pi f(x-\alpha+\psi, t+\alpha+\psi, \tau)d\psi\right). \qquad (6.24)
\end{aligned}$$

We have dropped the subscripts 0 in the variables x and t. Unimportant changes in the notation aside (our τ corresponds to Igoshin et al's variable T, $\mathcal{D}_x = 2\pi D_1$, $\mathcal{D}_\phi = 2\pi D_2$), these equations are different from those derived by Igoshin et al [22]: U and V in (6.21) are the same but Igoshin et al's Fokker-Planck equation lacks the source term $fQ[f]$. The reason is that Igoshin et al do not impose consistently the jump conditions (6.7)-(6.10) in their derivation; see their equations (A10)-(A.14) in the Appendix of [22]. The terms in (6.24) do not appear in these equations.

Equation (6.21) is a Fokker-Planck type equation with a source term $fQ[f] - \frac{\mathcal{D}_\phi}{\pi}\partial_x[f(x,t,\tau) - f(x-\pi, t+\pi, \tau)]$. Even in the absence of noise ($\mathcal{D}_x = \mathcal{D}_\phi = 0$), $fQ[f]$ acts as an effective *collision term* that produces dissipation. As we shall see in the next section, the source term provides a mechanism for wave number and speed selection of the ripples. No such mechanism was found in [22].

6.3 Constant Solution in the Weak Signaling Limit and its Linear Stability

The constant function $f = \hat{N}/(2\pi)$ is an exact solution of (6.21) that coincides with the following exact piecewise constant solution of the full model (3.12):

$$n_s(\phi) = p\,[\chi_{[0,\alpha]}(\phi) + \chi_{[-\pi,-\pi+\alpha]}(\phi)] + q\,[\chi_{[-\pi+\alpha,0]}(\phi) + \chi_{[\alpha,\pi]}(\phi)], \tag{6.25}$$

$$p = \frac{1+\epsilon\,\Omega\left(\frac{\hat{N}}{2}\right)}{\pi+\epsilon\alpha\,\Omega\left(\frac{\hat{N}}{2}\right)}\,\frac{\hat{N}}{2}, \quad q = \frac{\frac{\hat{N}}{2}}{\pi+\epsilon\alpha\,\Omega\left(\frac{\hat{N}}{2}\right)} \tag{6.26}$$

when $\epsilon = 0$. In (6.25), p and q given by (6.26) have been calculated from $N_\pm = \alpha p + (\pi - \alpha)q = \hat{N}/2$ and from the condition that the flux $J = n[1 + \epsilon\Omega(N_-)\chi_{[\alpha,\pi]} + \epsilon\Omega(N_+)\chi_{[-\pi+\alpha,0]})]$ should be continuous. Note that substitution of $f = \hat{N}/(2\pi)$ in

(6.14) yields

$$n_1^p = \begin{cases} \left(1-\frac{\alpha}{\pi}\right)\Omega\left(\frac{\hat{N}}{2}\right)\frac{\hat{N}}{2\pi}, & 0<\phi<\alpha \\ -\frac{\alpha}{\pi}\,\Omega\left(\frac{\hat{N}}{2}\right)\frac{\hat{N}}{2\pi}, & \alpha<\phi<\pi, \\ -\frac{\alpha}{\pi}\,\Omega\left(\frac{\hat{N}}{2}\right)\frac{\hat{N}}{2\pi}, & \alpha-\pi<\phi<0, \\ \left(1-\frac{\alpha}{\pi}\right)\Omega\left(\frac{\hat{N}}{2}\right)\frac{\hat{N}}{2\pi}, & -\pi<\phi<\alpha-\pi, \end{cases} \tag{6.27}$$

after using (6.16)-(6.18). Equation (6.27) agrees with (6.25)-(6.26) up to terms of order ϵ^2.

Let us see what we find by a linear stability analysis of $f = \hat{N}/(2\pi)$ as a solution of (6.21). Inserting $f = \hat{N}/(2\pi) + \nu(x,t,\tau)$ with $\nu \ll 1$ in (6.21) and keeping only terms that are linear in ν, we find

$$\begin{aligned} &\left[\partial_\tau - 2(\pi-\alpha)\,\Omega\left(\frac{\hat{N}}{2}\right)\partial_t - (\mathcal{D}_x+\mathcal{D}_\phi)\partial_x^2 - \mathcal{D}_\phi\partial_t^2\right]\nu = \frac{\hat{N}}{2\pi}\,\Omega'\left(\frac{\hat{N}}{2}\right) \\ &\times\left\{\partial_t\int_\alpha^\pi\int_0^\pi[\nu(x-\phi+\psi,t+\phi+\psi,\tau)+\nu(x+\phi-\psi,t+\phi+\psi,\tau)]d\psi d\phi\right. \\ &\quad-\partial_x\int_\alpha^\pi\int_0^\pi[\nu(x-\phi+\psi,t+\phi+\psi,\tau)-\nu(x+\phi-\psi,t+\phi+\psi,\tau)]d\psi d\phi \\ &\quad+\int_0^\pi[\nu(x+\psi,t-\psi,\tau)+\nu(x-\psi,t-\psi,\tau)-\nu(x+\alpha-\psi,t+\alpha+\psi,\tau) \\ &\qquad\left.-\,\nu(x-\alpha+\psi,t+\alpha+\psi,\tau)]\,d\psi\right\} - \frac{\mathcal{D}_\phi}{\pi}\partial_x[\nu(x,t,\tau)-\nu(x-\pi,t+\pi,\tau)]. \end{aligned} \tag{6.28}$$

Assuming $\nu = e^{ikx+ilt+\sigma\tau}$, we obtain the following eigenvalues:

$$\begin{aligned}\sigma &= 2il(\pi-\alpha)\,\Omega\left(\frac{\hat{N}}{2}\right) - (\mathcal{D}_x+\mathcal{D}_\phi)k^2 - \mathcal{D}_\phi l^2 + i2\hat{N}\,\Omega'\left(\frac{\hat{N}}{2}\right) \\ &\times \left\{ e^{i\pi l}\left[e^{i\alpha L}\sin[(\pi-\alpha)L]\frac{\sin(\pi K)}{2\pi K} + e^{i\alpha K}\sin[(\pi-\alpha)K]\frac{\sin(\pi L)}{2\pi L}\right]\right. \\ &\left. - e^{i\alpha L}\sin(\alpha L+\pi K)\frac{\sin(\pi K)}{2\pi K} - e^{i\alpha K}\sin(\alpha K+\pi L)\frac{\sin(\pi L)}{2\pi L}\right\} - \frac{ik\mathcal{D}_\phi}{\pi}(1-e^{i2\pi L}),\end{aligned} \tag{6.29}$$

where

$$K = \frac{l+k}{2}, \quad L = \frac{l-k}{2}. \tag{6.30}$$

For real k and l, the real and imaginary parts of (6.29) are

$$\begin{aligned}\operatorname{Re}\sigma &= -(\mathcal{D}_x+\mathcal{D}_\phi)k^2 - \mathcal{D}_\phi l^2 - \hat{N}\,\Omega'\left(\frac{\hat{N}}{2}\right)\left\{\sin(\alpha L+\pi l)\sin[(\pi-\alpha)L]\frac{\sin(\pi K)}{\pi K}\right. \\ &+ \sin(\alpha K+\pi l)\sin[(\pi-\alpha)K]\frac{\sin(\pi L)}{\pi L} - \sin(\alpha L)\sin(\alpha L+\pi K)\frac{\sin(\pi K)}{\pi K} \\ &\left. - \sin(\alpha K)\sin(\alpha K+\pi L)\frac{\sin(\pi L)}{\pi L}\right\} - \frac{k\mathcal{D}_\phi}{\pi}\sin(2\pi L),\end{aligned} \tag{6.31}$$

$$\begin{aligned}\operatorname{Im}\sigma &= 2l(\pi-\alpha)\,\Omega\left(\frac{\hat{N}}{2}\right) + \hat{N}\,\Omega'\left(\frac{\hat{N}}{2}\right)\left\{\cos(\alpha L+\pi l)\sin[(\pi-\alpha)L]\frac{\sin(\pi K)}{\pi K}\right. \\ &+ \cos(\alpha K+\pi l)\sin[(\pi-\alpha)K]\frac{\sin(\pi L)}{\pi L} - \cos(\alpha L)\sin(\alpha L+\pi K)\frac{\sin(\pi K)}{\pi K} \\ &\left. - \cos(\alpha K)\sin(\alpha K+\pi L)\frac{\sin(\pi L)}{\pi L}\right\} - \frac{2k\mathcal{D}_\phi}{\pi}\sin^2(\pi L),\end{aligned} \tag{6.32}$$

respectively. Except for the last two terms in (6.31), this is the same as (57) in [22] (with $\hat{N}$ replaced by $\hat{N}/2$) provided l is an integer. We have $\sigma = 0$ for $k = l = 0$ indicating that we can shift the constant solution $f = \hat{N}/(2\pi)$ by an arbitrary quantity. The integral condition (3.13) fixes the value of $\hat{N}$ and therefore we have to ignore the zero eigenvalue.

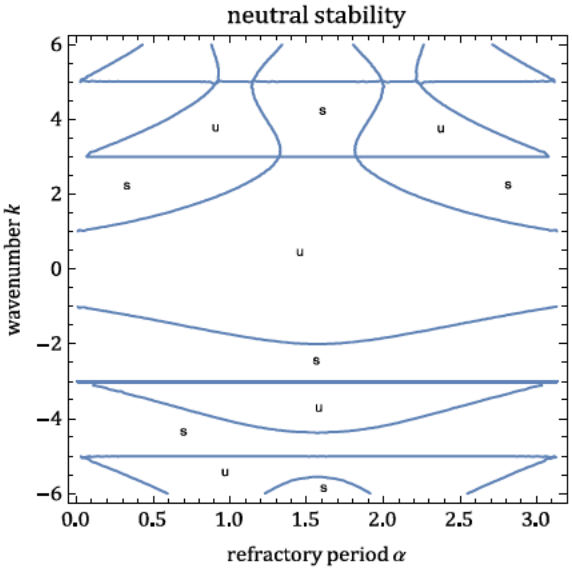

Fig 6.1: Contour plot of the neutral stability curve Re $\sigma(\alpha, k, 1) = 0$ for $0 \leq \alpha \leq \pi$, $-6 \leq k \leq 6$ and no diffusion, $\mathcal{D}_x = \mathcal{D}_\phi = 0$. Patterns are expected in regions where the constant solution is unstable (marked with "u") and they may disappear leaving the constant solution in regions where the latter is linearly stable (marked with "s").

Note that as $r \to \infty$, $\Omega'(\hat{N}/2) \to 0$ and the constant solution becomes stable according to (6.31). At bifurcation points, Re $\sigma = 0$, Im $\sigma \neq 0$. This suggests that a Hopf bifurcation occurs, which our numerical simulations support. Pattern solutions that are periodic in the slow time issue forth from the constant solution as *supercritical* Hopf bifurcations according to our numerical evidence. We have not found examples of subcritical Hopf bifurcations and hysteresis.

As $\epsilon \to 0$, $f(x, t, \tau)$ approaches (6.4), which is a 2π-periodic function of t. The corresponding frequency is $l = 1$. Figure 6.1 shows the contour plot of the neutral stability curve Re $\sigma(\alpha, k, 1) = 0$ in (6.31) for frequency $l = 1$ in the absence of diffusion, $\mathcal{D}_x = \mathcal{D}_\phi = 0$. The real part of the eigenvalue (6.31), Re $\sigma(\alpha, k, 1)$, is positive at the middle region enclosing $k = 0$ in Fig. 6.1 and its sign changes each time a line of the neutral stability curve is crossed. Thus, for unit frequency and $|k| \leq 1$, we expect to see patterns in x and t provided there is no diffusion. For any value of the refractory period α, the constant solution is unstable for waves traveling to the left ($k = -1$) and also for waves traveling to the right ($k = 1$). Let us assume that the initial condition is a periodic pattern of wave number $k > 0$. Increasing the wave number k or adding diffusion (which may be the result of unavoidable numerical errors) stabilize the constant solution and cause the patterns to disappear. For a fixed value of the refractory period α, the neutral stability curve of Fig. 6.1 yields the critical wave number below which patterns with that wave number appear. Similarly, increasing the refractory period from $\alpha = 0$ at a fixed wave number $1 < k < 3$ should produce patterns with wave number k once α surpasses the critical value given by the neutral stability curve.

For other values of the frequency, the neutral stability curve qualitatively changes. For instance, let us consider wave trains traveling to the right, so that $k = -l$, $L = l$, $K = 0$, as in [22]. (6.31) becomes

$$\begin{aligned}\text{Re}\,\sigma &= -(\mathcal{D}_x + 2\mathcal{D}_\phi)l^2 - \hat{N}\,\Omega'\left(\frac{\hat{N}}{2}\right)\left\{\sin[(\alpha+\pi)l]\sin[(\pi-\alpha)l] - \sin^2(\alpha l)\right\} + \frac{l\mathcal{D}_\phi}{\pi}\sin(2\pi l)\\ &= -\mathcal{D}_x l^2 - \frac{l\mathcal{D}_\phi}{\pi}[2\pi l - \sin(2\pi l)] + \hat{N}\,\Omega'\left(\frac{\hat{N}}{2}\right)[2\sin^2(\alpha l) - \sin^2(\pi l)], \qquad (6.33)\end{aligned}$$

$$\begin{aligned}\text{Im}\,\sigma &= 2l(\pi-\alpha)\Omega\left(\frac{\hat{N}}{2}\right) + \hat{N}\Omega'\left(\frac{\hat{N}}{2}\right)\left\{\cos[(\pi+\alpha)l]\sin[(\pi-\alpha)l] - \frac{1}{2}\sin(2\alpha l)\right.\\ &\quad \left. - \frac{\sin^2(\pi l)}{\pi l}\right\} + \frac{2l\mathcal{D}_\phi}{\pi}\sin^2(\pi l) = 2l(\pi-\alpha)\,\Omega\left(\frac{\hat{N}}{2}\right) + \frac{\hat{N}}{2}\,\Omega'\left(\frac{\hat{N}}{2}\right)\left[\sin(2\pi l)\right.\\ &\quad \left. - \frac{2\sin^2(\pi l)}{\pi l} - 2\sin(2\alpha l)\right] + \frac{2l\mathcal{D}_\phi}{\pi}\sin^2(\pi l). \qquad (6.34)\end{aligned}$$

In absence of diffusion, $\mathcal{D}_x = \mathcal{D}_\phi = 0$, (6.33) shows that Re $\sigma = 0$ for $l = l_c(\alpha)$ such that $2\sin^2(\alpha l) = \sin^2(\pi l)$. This $l_c(\alpha)$ provides the wavelength of the observed patterns. The contour plot of Re $\sigma = 0$ in Fig. 6.2 shows that the function $l_c(\alpha)$ is multivalued and that its leftmost branch (corresponding to the lowest values of $l > 0$) decreases from $\alpha = \pi/\sqrt{2}$ at $l = 0$ to 0 at $l = 1$. For this parameter range, the constant solution is linearly stable if $l < l_c(\alpha)$ and unstable for $l > l_c(\alpha)$ (but smaller than values at the next branch of $l_c(\alpha)$). For sufficiently small l, α smaller (larger) than a critical value corresponds to stable (unstable) constant solution. As

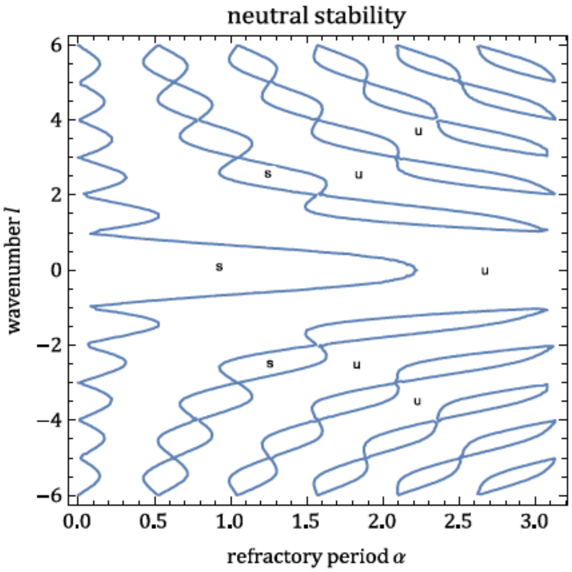

Fig 6.2: Contour plot of the neutral stability curve $Re\ \sigma(\alpha, -l, l) = 0$ (waves traveling to the right) for $0 \leq \alpha \leq \pi$, $-6 \leq l \leq 6$, and $\mathcal{D}_x = \mathcal{D}_\phi = 0$. Meaning of "s" and "u" as in *Fig 6.1*.

the exponent r increases and $\Omega'(\hat{N}/2)$ correspondingly decreases, the contribution of the second term in (6.33) becomes smaller and can be obliterated by diffusion or numerical noise even if the said term is positive.

6.4 Numerical Solutions

In this section, we present numerical solutions of the full kinetic model equations (3.1) - (3.6) and compare them with the linear stability results for the Fokker-Planck type equation (6.21) derived in the weak signaling limit. To visualize the results, we obtain the total density, $N_+(x,t) + N_-(x,t)$, and the RPD, $n_{\mathrm{RPD}}(x,t)$, from the numerical solution.

We construct the numerical solution using uniform grids for both the spatial variable x and the phase variable ϕ extended over their whole domains and assigning an approximate value of the solution on every point of the two-dimensional grid at every time step. In all our calculations in this chapter we use $N = 100$ subintervals in both space and phase and set $\mathcal{L} = \pi$, $r = 4$. Then we solve the noiseless nondimensional equations, (3.12) (with $\mathcal{D}_x = \mathcal{D}_\phi = 0$), using as basic scheme an upwind finite difference scheme in conservation form for the spatial terms (space and phase) and the Euler explicit algorithm to evolve in time. We have formulated a high order accurate version in space and time based on the fifth-order weighted essentially nonoscillatory reconstruction procedure (WENO5) for the spatial variables and a third-order Runge-Kutta method to evolve in time.

The computation of the integral form of the fluxes for the internal clock variable is performed through the trapezoidal rule of numerical integration extended over the whole domain of the phase variable, using the approximated values of the solution at the grid points. All these methods are explained in Chapters 4 and 5.

If $\epsilon = 0$ the hyperbolic system (3.1)-(3.6) becomes a system of linear wave equations and the numerical solution can be approximated using standard upwind schemes of any order of accuracy in space and time. When nonlinearity is present, $\epsilon > 0$, the solution might present wave steepening but the non-locality of the flux in Eq. (3.3) introduces an analytic dissipation mechanism. Then even for zero-diffusion, the solution is well defined and plain upwind schemes converge stably to it. The jump conditions (6.7)-(6.10) may enforce continuity at the boundaries $\phi = \pm\pi$, 0, α, $\alpha - \pi$, but wave steepening can be generated in the spatial direction of the solution for short periods of time. On the other hand, we do not have numerical evidence of shock wave formation. The dissipation mechanism introduced by the non-local fluxes might prevent the formation of shock waves. This issue will be examined in the near future.

Igoshin et al [21] use a heuristic argument to suggest that $k_c = 1$ and estimate $\epsilon = 3$, $\alpha = \pi/5$ from their measurements. The values of ϵ determine where the solution is closed to the weak signaling limit: $\epsilon = 0.1$ corresponds to the weak signaling limit and larger values, such as $\epsilon = 3$ [21], or $\epsilon = 10$, go beyond the Fokker-Planck type description of Section 6.3. To check the stability results of that section, we first solve the nondimensional equation (3.12) with the following initial condition that is periodic in x and ϕ: $n(x, \phi, t = 0) = 1 + 0.1 \sin(kx) \sin(\phi)$ on the interval $[-\pi, \pi] \times [-\pi, \pi]$. For a first numerical simulation, we consider the case of $\epsilon = 0.1$ and a fixed $\alpha = \pi/2$. In Figure 6.3, we show the time-space surface plots of the total density with $k = 1$, $k = 4$, and $k = 6$ from left to right. As expected from the neutral stability curve of Fig. 6.1, the simulations of Fig. 6.3 show that periodic patterns with angular frequency $l = 1$ are found for $k = 1$, whereas the uniform stationary solution is linearly stable if $k = 4$. Fig. 6.3(b) shows a transient stage towards this solution. At $k = 6$, the uniform stationary solution is unstable to periodic patterns. However, simulations

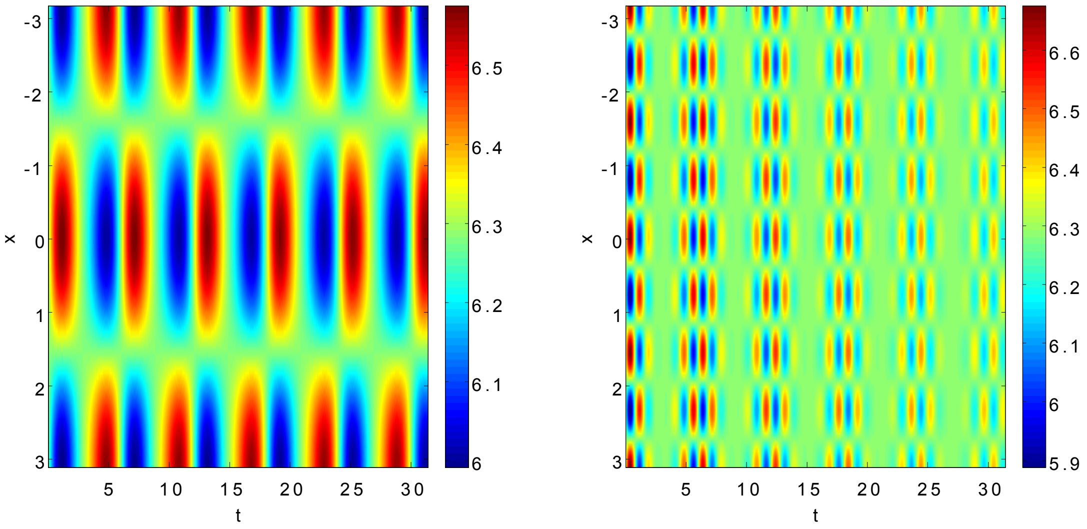

(a) $k = 1$

(b) $k = 4$

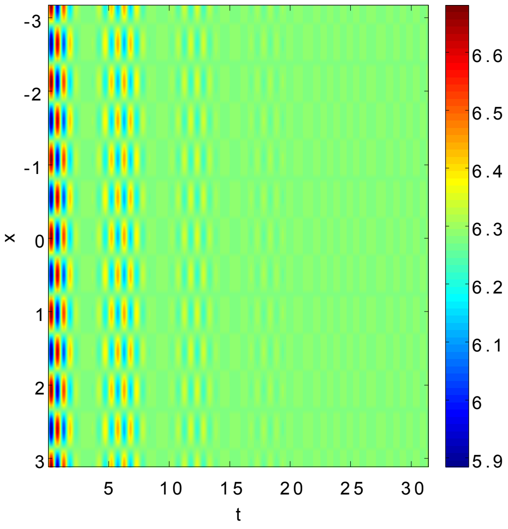

(c) $k = 6$

Fig 6.3: Contour plot of the total density $N_+(x,t) + N_-(x,t)$ for $\alpha = \pi/2$, $\epsilon = 0.1$ and wavenumber: (a) $k = 1$, (b) $k = 4$, (c) $k = 6$.

show an even faster transient to the uniform stationary solution. According to (6.31), noise has a strongly stabilizing effect of this solution at high wavenumber so that numerical noise might have obliterated the pattern solution at $k = 6$.

The RPD exhibits the same behavior as the total density and its contour plot (not shown) is quite similar to it. In Figure 6.4, we depict the RPD at $x = 0$ for the same values of the parameters. For unit wavenumber, periodic patterns are stable. The slight decrease of the maxima of the RPD observed in Fig. 6.4(a) is due to unavoidable dissipation due to numerical errors. For $k = 4$, the uniform stationary solution is stable according to the neutral stability curve of Fig. 6.1. Fig. 6.4(b) shows a pronounced evolution towards a constant. However, as we are not far from the bifurcation point (critical wavenumbers bounding the stability region for the uniform stationary solution are 3 and 5), the evolution of the RPD towards a constant value is slow. For $k = 6$, neutral stability predicts periodic patterns. However at such large wavenumber, the dissipation due to numerical noise is so large that the pattern disappears and the uniform stationary solution becomes stable, as shown in Fig. 6.4(c).

Other patterns appear for different initial conditions. For example, for an initial condition with constant density for all x except for two bumps near $x = \pm\pi$, $n(x, \phi, 0) = 1.5 + [H(x - \pi + a) - H(x - \pi)] + [H(x + \pi) - H(x + \pi - a)]$, $a = \pi/10$ [$H(x) = 1$ for $x > 0$, and $H(x) = 0$ otherwise], we obtain the *standing wave patterns* shown in Fig. 6.5. Reversals get confined to regions near $x = \pm\pi$ as the nonlinearity

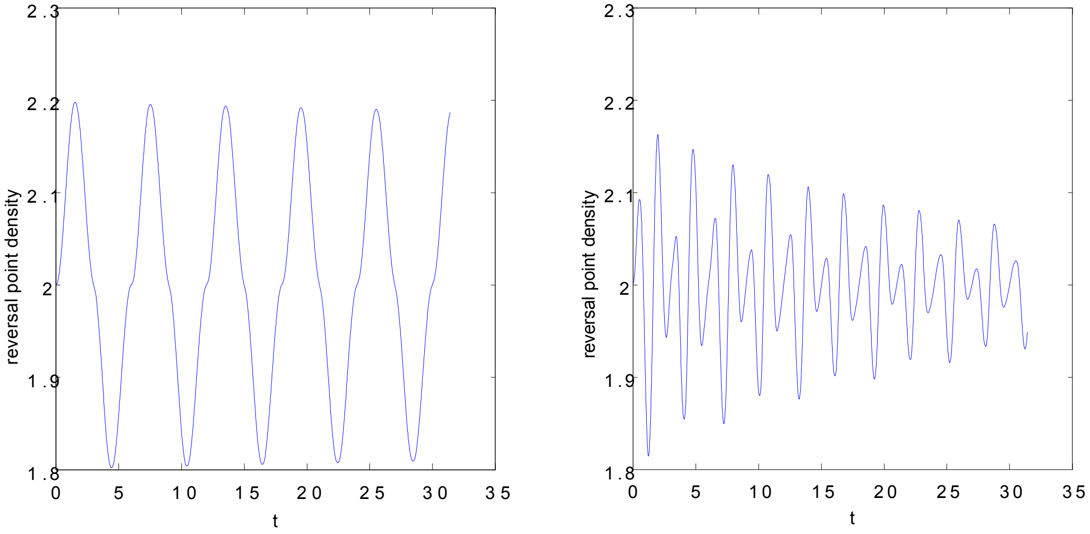

(a) $k = 1$

(b) $k = 4$

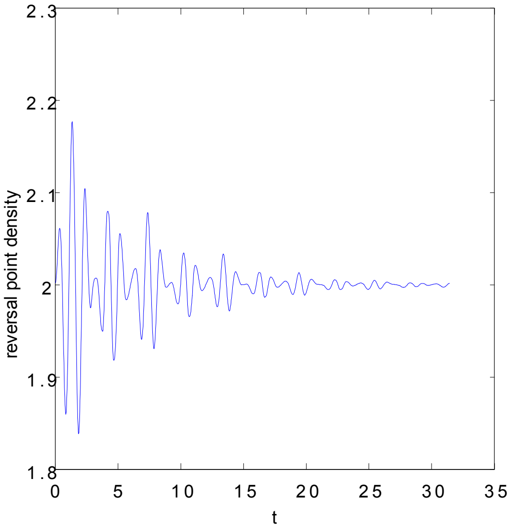

(c) $k = 6$

Fig 6.4: Plots of the RPD, $n_{RPD}(x = 0, t)$, vs. time for $\alpha = \pi/2$, $\epsilon = 0.1$ and wavenumber: (a) $k = 1$ (stable periodic pattern), (b) $k = 4$ (transient to constant density), (c) $k = 6$ (faster transient to constant density).

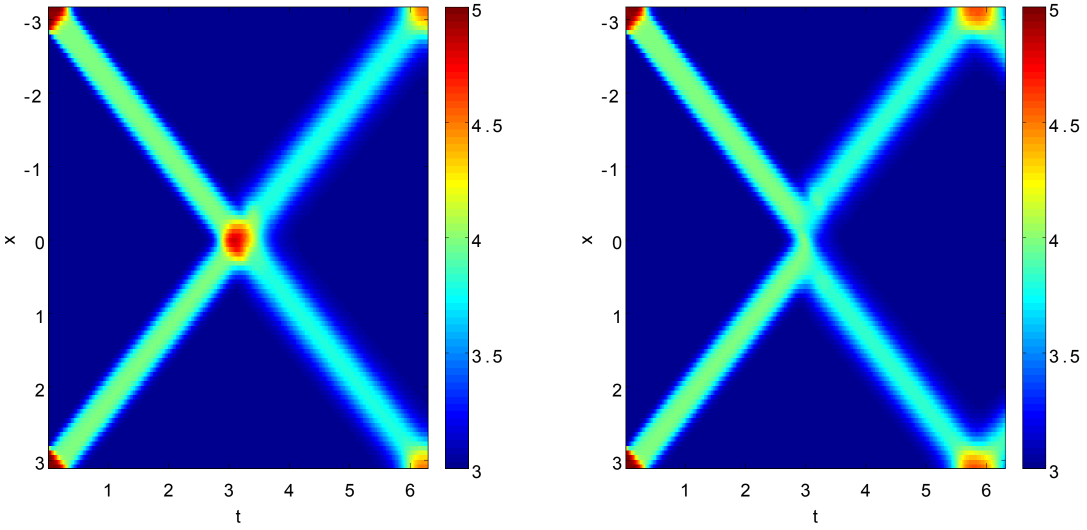

(a) $\epsilon = 0$ (b) $\epsilon = 0.1$

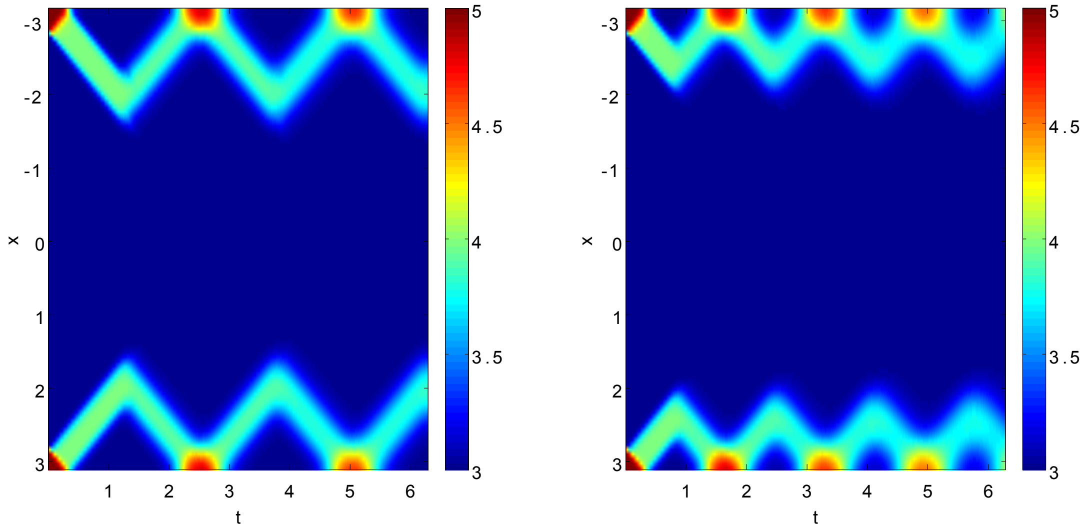

(c) $\epsilon = 3$ (d) $\epsilon = 12$

Fig 6.5: Contour plots of the RPD, $n_{RPD}(x,t)$, for $\alpha = \pi/5$, initial condition $n(x,\phi,0) = 1.5 + [H(x-\pi+a) - H(x-\pi)] + [H(x+\pi) - H(x+\pi-a)]$, $a = \pi/10$, and: (a) $\epsilon = 0$, (b) $\epsilon = 0.1$, (c) $\epsilon = 3$, (d) $\epsilon = 12$. As ϵ (nonlinearity) increases, the reversals occur closer to $\pm\pi$.

strength ϵ increases. For larger values of ϵ, the weak signaling theory of Sections 6.2 and 6.3 does not apply.

If the two bumps are closer, then the standing waves generate local maxima as in Fig. 6.6(a) and (b), for $\epsilon = 0$ and 1.2, respectively. As ϵ (nonlinearity) increases, the reversals occur in smaller regions about $x = \pm\pi/2$, as shown in Figs. 6.6(c) and (d). Clearly, for bumps that are close enough, the waves they issue reinforce the density at the points where they cross. In these points, fruiting bodies may form [21]. It is interesting to observe that breaking the symmetry in the initial condition may weaken the resulting patterns. For example replacing the initial condition in Fig. 6.6 by $n(x, \phi, 0) = 1.5 + [H(x - \pi/2 + a) - H(x - \pi/2)] + [H(x + \pi/2) - H(x + \pi/2 - a)]$ (closer and narrower bumps, with centers at $\pi/2 - a/2$ and $-\pi/2 + a/2$) results in patterns with two close maxima appearing near $t = n\pi$ $(n = 1, 2, \ldots)$ that undergo noticeable dissipation.

For analyzing a nonsymmetrical case, we take the initial condition $n(x, \phi, 0) = 1.5 + 0.1[H(\pi/2 - x) - H(\pi/2 + \pi/5 - x)]$ (see Fig. 6.7) with one bump with center at $\pi/2 + \pi/10$. We can observe that, as ω_1 increases, the resulting patterns confine at $\pi/2 + \pi/10$, where the reversals occur.

For an initial condition $n(x, \phi, 0) = 1.5 + 0.1 \sin[k(x - \phi)]$, $\alpha = \pi/5$, the *standing wave patterns* shown in Fig. 6.8(a) become the *traveling wave time periodic patterns* of Figs. 6.8(b) and 6.8(c).

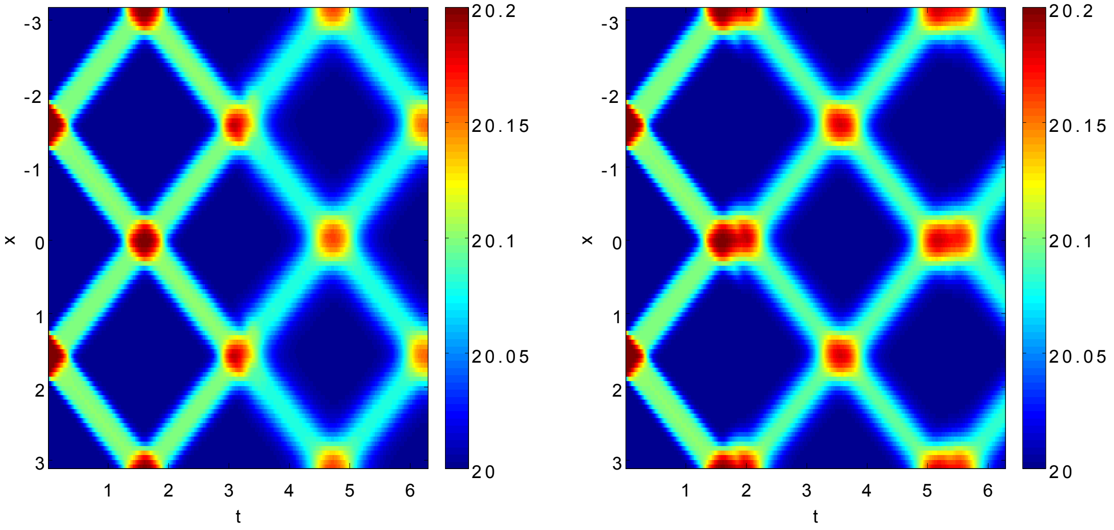

(a) $\epsilon = 0$ (b) $\epsilon = 1.2$

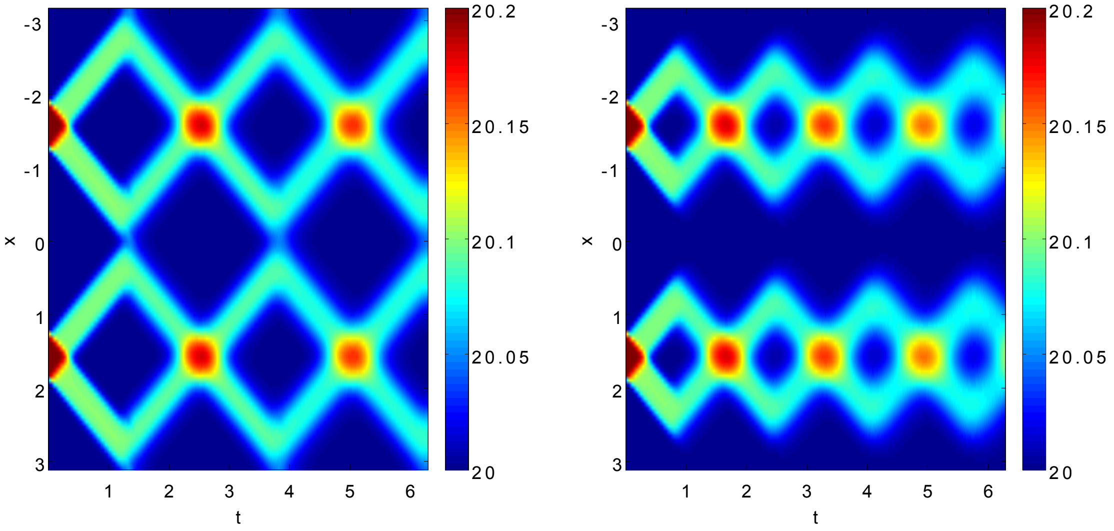

(c) $\epsilon = 3$ (d) $\epsilon = 12$

Fig 6.6: Contour plots of the RPD, $n_{RPD}(x,t)$, for $\alpha = \pi/5$, initial condition $n(x,\phi,0) = 10 + 0.1[H(a - |x - \pi/2|) + H(a - |x + \pi/2|)]$, $a = \pi/10$, and: (a) $\epsilon = 0$, (b) $\epsilon = 1.2$, (c) $\epsilon = 3$, (d) $\epsilon = 12$. As ϵ (nonlinearity) increases, the reversals occur in smaller regions about $x = \pm\pi/2$.

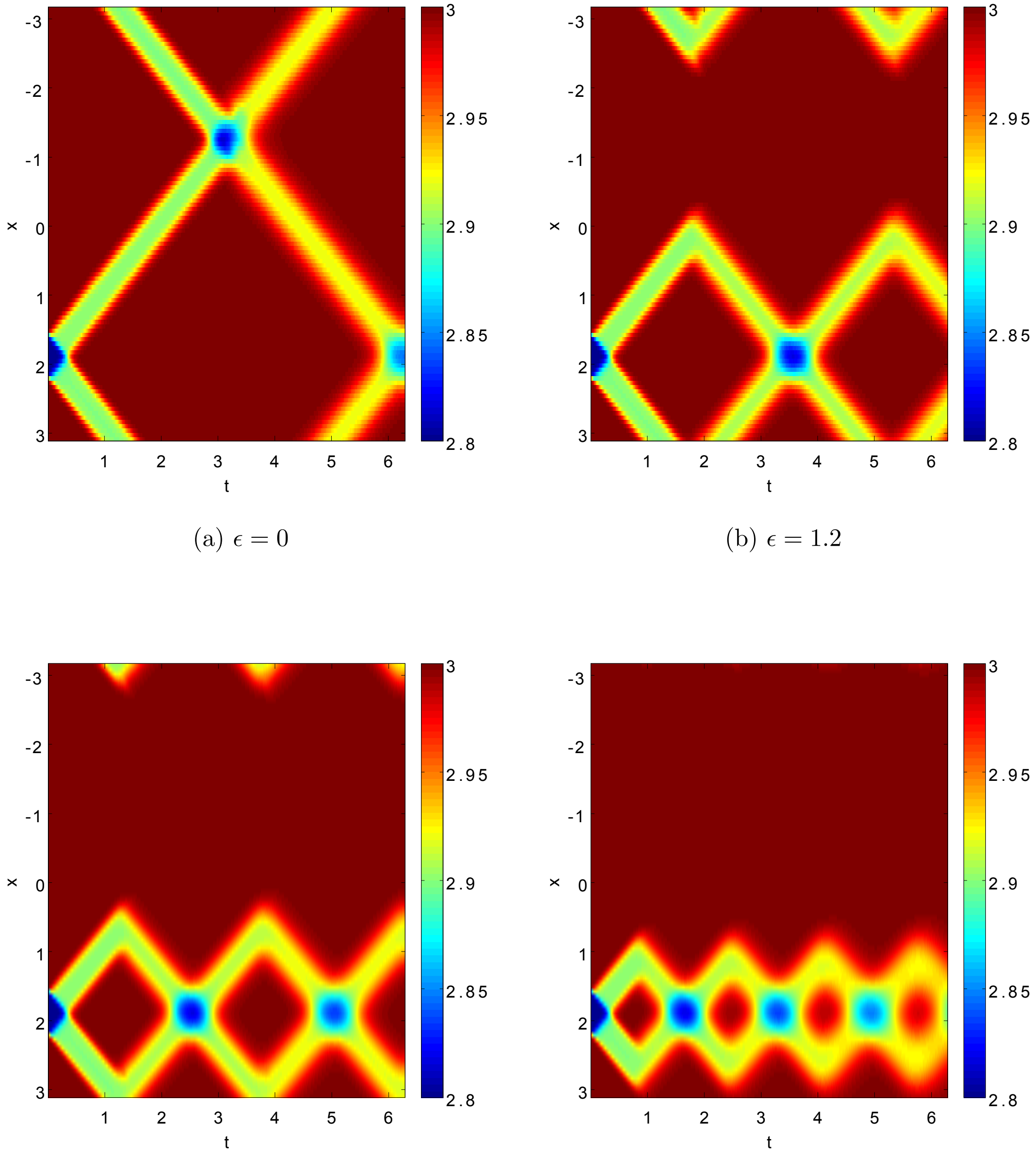

(a) $\epsilon = 0$

(b) $\epsilon = 1.2$

(c) $\epsilon = 3$

(d) $\epsilon = 12$

Fig 6.7: Contour plots of the RPD, $n_{RPD}(x,t)$, for $\alpha = \pi/5$, initial condition $n(x,\phi,0) = 1.5 + 0.1[H(\pi/2 - x) - H(\pi/2 + \pi/5 - x)]$, and: (a) $\epsilon = 0$, (b) $\epsilon = 1.2$, (c) $\epsilon = 3$, (d) $\epsilon = 12$.

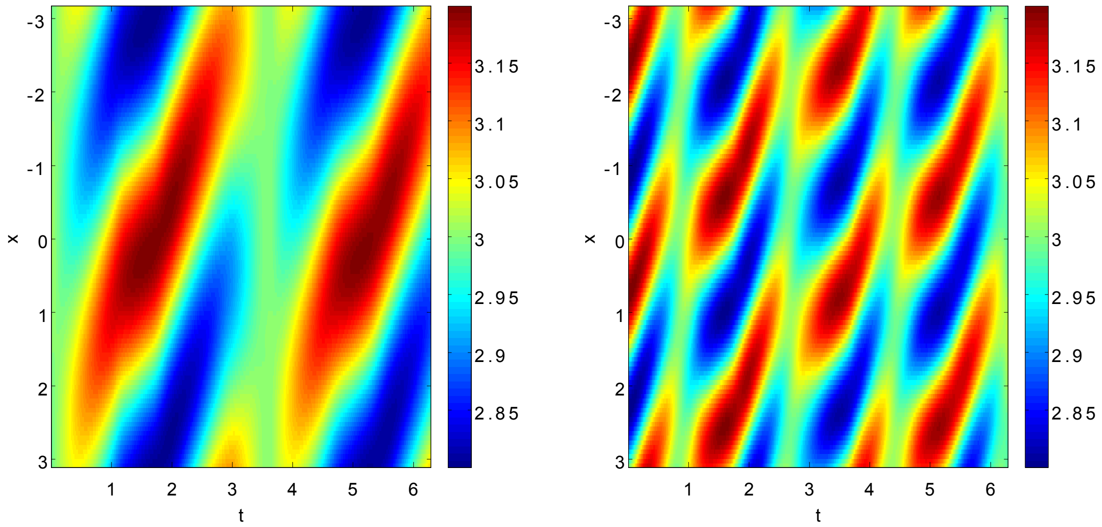

(a) $k = 1$ (b) $k = 2$

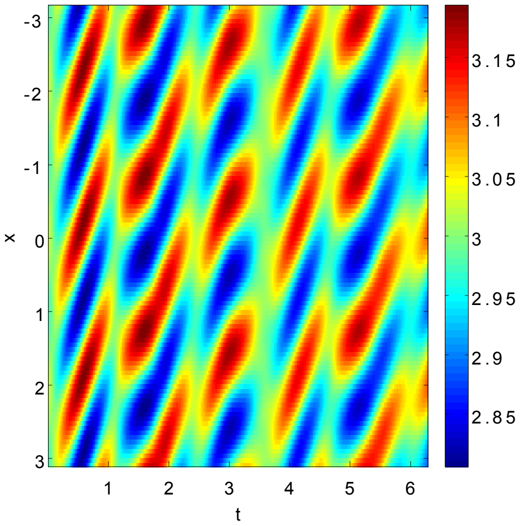

(c) $k = 3$

Fig 6.8: Contour plots of the RPD, $n_{RPD}(x,t)$, for $\alpha = \pi/5$, initial condition $n(x,\phi,0) = 1.5 + 0.1\sin[k(x-\phi)]$, $\epsilon = 1.2$, and: (a) $k = 1$, (b) $k = 2$, (c) $k = 3$. As k (wavenumber) increases, standing-wave time-periodic patterns become traveling-wave time-periodic patterns.

Relation to patterns observed in experiments The Igoshin et al model we have solved numerically is 1D whereas observed patterns are 2D. This said, the complete patterns in panels (a) and (b) of Figures 6.5 and 6.6 are similar to those in Figure 3 of Welch and Kaiser's experiments [68], whereas loss of coherence (panels (c) and (d) of our Figures 6.5 and 6.6) is observed in Figures 3(a) and 4 of the same work. Experiments also show more complex 2D patterns as in Figure 4 of [4] that are reminiscent of our patterns in Fig. 6.8 although the 2D agent-based models the authors of [4] introduce to explain the experiments are more sophisticated than the 1D model we study in this paper.

6.5 Pattern Decoherence and Relation to the Kuramoto Model

The noiseless version of Igoshin et al's model (3.1)-(3.6) describes the density of myxobacteria with an internal clock in the limit as the number of bacteria $\mathcal{N} \to \infty$. The bacteria themselves satisfy the following equations

$$\dot{x}_j = v \,\mathrm{sign}\phi_j, \tag{6.35}$$

$$\dot{\phi}_j = \omega + \epsilon\omega\, \Omega(N_{\mathrm{sign}(-\phi_\mathrm{j})}(x_j, t))[\chi_{[\alpha,\pi]}(\phi_j) + \chi_{[-\pi+\alpha,0]}(\phi_j)], \quad j = 1, \dots, \mathcal{N}, \tag{6.36}$$

$$N_+(x,t) = \frac{\nu_s}{\mathcal{N}} \sum_{m=1}^{\mathcal{N}} \delta(x - x_m(t))\, H(\phi_m(t)), \quad N_- = \frac{\nu_s}{\mathcal{N}} \sum_{m=1}^{\mathcal{N}} \delta(x - x_m(t))\, H(-\phi_m). \tag{6.37}$$

Here $x_j(t)$ and $\phi_j(t)$ move on circles and can be considered to take values on the intervals $[-L, L]$ and $[-\pi, \pi]$, respectively, ν_s is a scaling parameter, and the delta functions are regularized in an appropriate way. In the limit as we take away this regularization and $\mathcal{N} \to \infty$, the densities (6.37) approach their continuum limits (3.5). A typical bacterium $x_j(t)$ moves counterclockwise on a circle of length $2L$ if its internal phase $\phi_j(t) \in [-\pi, \pi]$ is positive, and clockwise otherwise. Its internal phase can be accelerated due to a mean-field interaction with opposite moving bacteria that collide with it. Appropriate initial conditions produce periodic (rhythmic) spatiotemporal patterns in the absence of interaction ($\epsilon = 0$). Interaction tends to confine rhythmicity to parts of the circle $(-L, L)$, as shown in Figures 6.5 and 6.8, or to destroy it. Loss of rhythmicity may appear as a *decoherence* phase transition at critical values of the refractory period α or the wavenumber of the initial condition, as shown in Figs. 6.3 and 6.4. The maxima of the time derivative of the reversal point density act as the order parameter for this phase transition: it is zero for the constant density solution and nonzero for the time-periodic patterns, see Fig. 6.4 (c).

The behavior of this model can be compared with the well-known Kuramoto model of globally coupled phase oscillators [1, 35]. In the Kuramoto model, the phases of free oscillators increase following their natural frequencies that are random (unsynchronized or incoherent state). Mean-field coupling between the oscillators succeed synchronizing them above a certain coupling strength and, typically, some oscillators are synchronized while others continue rotating about the unit circle (partial synchronization). In the Igoshin et al's model, a pattern induced by an appropriate initial condition persists in the absence of coupling. Turning on the coupling may confine the patterns to a part of the space interval $[-L, L]$ (partial decoherence) or destroy them completely (complete decoherence). Adding white noise sources, the Kuramoto model is described by a nonlinear Fokker-Planck equation whereas the Igoshin et al's model contain extra mechanisms of dissipation, as it is apparent from the nonlinear Fokker-Planck equation with an additional (collision) source term (6.21) obtained in the weak signaling limit.

6.6 Conclusions

We have revisited the continuum model of rippling in myxobacteria proposed by Igoshin et al [21, 22]. In the absence of noise, the model consists of two coupled hyperbolic equations (describing the densities of left and right moving bacteria) coupled nonlinearly through a flux in an angular variable that represents the bacteria internal clock. This flux is a nonlinear function of the overall density of left or right moving bacteria. Depending on the values of the parameters, the model displays a variety of space and time periodic patterns that have been scarcely analyzed.

In the limit of weak nonlinearity (weak signaling), we have found a Fokker-Planck type equation for the reversal-point density that contains a source term, absent in Igoshin et al's analysis [22]. The reversal-point density can be used to reconstruct the densities of left and right moving bacteria. We analyze the linear stability of a constant-density solution and find that its neutral stability curves provide selection rules giving the wavenumber of the patterns issuing from the constant-density solution. These selection rules issue directly from the source term in the Fokker-Planck equation. We have checked these results by direct numerical solution of the original hyperbolic equations of the model. For small nonlinearities, we have checked the wavenumber selection rule. Strengthening the nonlinearity tends to confine and destroy the patterns through a nonequilibrium phase transition. For large nonlinearity, we have found a variety of patterns including time-periodic standing and traveling waves that attest the richness of Igoshin et al's model.

Chapter 7. Conclusions

We have revisited the continuum model of rippling in myxobacteria proposed by Igoshin et al [21], [22].

In the absence of noise, the model consists of two coupled hyperbolic equations (describing the densities of left and right moving bacteria) coupled nonlinearly through a flux in an angular variable that represents the bacteria internal clock. The flux is a nonlinear function of the overall density of left or right moving bacteria. Depending on the values of the parameters, the model displays a variety of space and time periodic patterns that have been analyzed.

We have solved numerically the model without diffusion operator, and the role of the nonlocal advection operator as generator of dissipation was shown by the analysis of the weakly nonlinear limit and by solving the equation using a high order accurate numerical schemes. We have used two hyperbolic reconstructions (piecewise hyperbolic method and power piecewise hyperbolic method) and another two parabolic reconstructions (weighted essentially nonoscillatory method and weighted power essentially nonoscillatory method) in order to reproduce the pattern behavior from myxobacteria rippling. With these high-precision numerical tools we can maintain the amplitude of the traveling myxobacteria waves, and without adding analytical dissipation, we were capable to reproduce the pattern of myxobacteria due to the small numerical dissipation. Using these numerical approximations for the case when the signaling is strong, we were able to analyze the parameters of the model to locate Hopf bifurcations.

In the limit of weak signaling, we have found a Fokker-Planck type equation for the reversal-point density that contains a source term, absent in Igoshin et al's analysis [22]. The reversal point density can be used to reconstruct the densities of left and right moving bacteria. We analyzed the linear stability of a constant-density solution and found that its neutral stability curves provide selection rules giving the wavenumber of the patterns issuing from the constant-density solution. These selection rules issue directly from the source term in the Fokker-Planck equation. We have checked these results by direct numerical solution of the original hyperbolic equations of the model. The behavior of this model can be compared with the well-known Kuramoto model of globally coupled phase oscillators, but this prospective research is expected to be developed in the near future.

References

[1] J. A. Acebrón, L. L. Bonilla, C. J. Pérez Vicente, F. Ritort and R. Spigler, *The Kuramoto model: a simple paradigm for synchronization phenomena.* Rev. mod. Phys. 77, 137-185 (2005)

[2] M. S. Alber, Y. Jiang and M. A. Kiskowski, *Lattice gas cellular automation model for rippling and aggregation in myxobacteria.* Physica D 191, 343-358 (2004)

[3] A. R. A. Anderson and B. N. Vasiev, *An individual based model of rippling movement in a myxobacteria population.* J. theor. Biol. 234, 341-349 (2005)

[4] R. Balagam and O. A. Igoshin, *Mechanism for Collective Cell Alignment in Myxococcus xanthus Bacteria.* PLoS Comp. Biology 11(8), e1004474 (2015)

[5] R. Balagam, D. B. Litwin, F. Czerwinski, M. Sun, H. B. Kaplan, J. W. Shaevitz and O. A. Igoshin, *Myxococcus xanthus Gliding Motors Are Elastically Coupled to the Substrate as Predicted by the Focal Adhesion Model of Gliding Motility.* PLoS Comput Biol 10(5): e1003619 (2014)

[6] E. Ben-Jacob, I. Cohen and H. Levine, *Cooperative self-organization of microorganisms.* Adv. Phys. 49, 395-554 (2000)

[7] U. Börner and M. Bär, *Pattern formation in a reaction-advection model with delay: a continuum approach to myxobacterial rippling.* Ann. Phys. 13, 432-441 (2004)

[8] U. Börner, A. Deutsch, H. Reichenbach and M. Bär, *Rippling patterns in aggregates of myxobacteria arise from cell-cell collisions.* Phys. Rev. Lett. 89, 078101 (2002)

[9] J. Crank and P. Nicolson, *A practical method for numerical evaluation of solution of partial differential equations of the heat conduction type.* Proc. Camb. Philos. Soc. 43, 50-67 (1947)

[10] E. Eckhert, P. Rangamani, A. E. Davis, G. Oster and J. E. Berleman, *Dual Biochemical Oscillators May Control Cellular Reversals in Myxococcus xanthus.* Biophys J. 107(11), 2700-2711 (2014)

[11] A. Gallegos, B. Mazzag and A. Mogilner, *Two continuum models for the spreading of myxobacteria swarms.* Bull. Math. Biol. 68, 837-861 (2006)

[12] S. K. Godunov, *A Finite Difference Method for the Numerical Computation of Discontinuous Solutions of the Fluid Dynamics.* Matematicheskii Sbornik 47, 271-306 (1959)

[13] A. Harten, *High resolution schemes for hyperbolic conservation laws.* J. Comput. Phys. 49, 357-393 (1983)

[14] A. Harten, B. Engquist, S. Osher and S. Chakravarthy, *Uniformly High-Order Accurate Essentially Non-Oscillatory Schemes III.* Journal of Computational Physics 71, 231-303 (1987)

[15] A. Harten and S. Osher, *Uniformly High-Order Accurate Non-Oscillatory Schemes I.* SIAM Journal on Numerical Analysis 24, 279-309 (1987)

[16] C. W. Harvey, M. Alber, L. S. Tsimring and I. S. Aranson, *Continuum modeling of myxobacteria clustering.* New Journal of Physics 15, 035029 (2013)

[17] M. Hendrata and B. Birnir, *Dynamic-energy-budget-driven fruiting-body formation in myxobacteria.* Physical Review E 81, 061902 (2010)

[18] M. Hendrata, Z. Yang, R. Lux and W. Shi*, Experimentally guided computational model discovers important elements for social behavior in myxobacteria.* PloS One 6, e22169 (2011)

[19] J. Henrichsen, *Bacterial surface translocation: a survey and classification.* Bacterial Rev. 36, 478-503 (1972)

[20] T. Hofer, J. A. Sherratt and P. K. Maini, *Dictyostelium discoideum: cellular self-organisation in an excitable biological medium.* Proc. R. Soc. Lond. B 259, 249-257 (1995)

[21] O. A. Igoshin, A. Mogilner, R. D. Welch, D. Kaiser and G. Oster, *Pattern formation and traveling waves in myxobacteria: Theory and modeling.* Proc. Natl. Acad. Sci. USA 98, 14913-14918 (2001)

[22] O. A. Igoshin, J. C. Neu and G. Oster, *Developmental waves in myxobacteria: A distinctive pattern formation mechanism.* Phys. Rev. E 70, 041911 (2004)

[23] O. A. Igoshin, R. Welch, D. Kaiser and G. Oster, *Waves and aggregation patterns in myxobacteria.* Proc. Natl. Acad. Sci. USA 101, 4256-4261 (2004)

[24] A. Janulevivius, M. von Loosdrecht, C. Picioreanu, *Short-range guiding can result in the formation of circular aggregates in myxobacteria populations.* PLoS Comput Biol 11(4) e1004213 (2015)

[25] L. Jelsbak and L. Søgaard-Andersen, *The cell surface-associated intercellular Csignal induces behavioral changes in individual Myxococcus xanthus cells during fruiting body morphogenesis.* Proceedings of the National Academy of Sciences of the United States of America 96, 5031-5036 (1999)

[26] L. Jelsbak and L. Søgaard-Andersen, *Cell behavior and cell-cell communication during fruiting morphogenesis in Myxococcus xanthus.* J. Microbiol. Methods 55, 829-839 (2003)

[27] G.-S. Jiang and C.-W. Shu, *Efficient implementation of weighted ENO schemes.* Journal of Computational Physics 126, 202-228 (1996)

[28] D. Kaiser, *Coupling cell movement to multicellular development in myxobacteria.* Nature Reviews Microbiology 1, 45–54 (2003)

[29] D. Kaiser, *Signaling in myxobacteria.* Annual Review of Microbiology 58, 75-98 (2004)

[30] D. Kaiser and C. Crosby, *Cell movement and its coordination in swarms of Myxococcus xanthus.* Cell Motility 3, 227-245 (1983)

[31] D. Kaiser, M. Robinson and L. Kroos, *Myxobacteria, Polarity, and Multicellular Morphogenesis.* Cold Spring Harbor Perspectives in Biology 2(8), a000380 (2010)

[32] D. Kaiser and H. Warrick, *M. xanthus swarms are driven by growth and regulated by a pacemaker.* J. Bacteriol. 193, 5898-5904 (2011)

[33] K. Kim and D. Kaiser, *C-factor: A cell-cell signaling protein required for fruiting body morphogenesis of M. xanthus.* Cell 61, 19-26 (1990)

[34] K. Kim and D. Kaiser, *Cell motility is required for the transmission of C-factor, an intercellular signal that coordinates fruiting body morphogenesis of Myxococcus xanthus.* Genes Dev. 4, 896-904 (1990)

[35] Y. Kuramoto, *Self-entrainment of a population of coupled nonlinear oscillators.* In International Symposium on Mathematical Problems in Theoretical Physics, H. Araki ed. Lecture Notes in Physics 39, Springer, N.Y., 420-422 (1975)

[36] P. D. Lax and B. Wendroff, *Systems of Conservation Laws.* Appl. Math. 13, 217-237 (1960)

[37] B. van Leer, *Towards the Ultimate conservative Difference Scheme IV. A new approach to Numerical Convection.* J. Comp. Phys. 23, 276-299 (1997)

[38] X-D. Liu, S. Osher and T. Chan, *Weighted essentially non-oscillatory schemes.* J. Comput. Phys. 115, 200-212 (1994)

[39] F. Lutscher and A. Stevens, *Emerging patterns in hyperbolic model for locally interacting cell systems.* J. Nonlinear Sci. 12, 619-640 (2002)

[40] P. Maini, *Using mathematical models to help understand biological pattern formation.* C. R. Biologies 327, 225-234 (2004)

[41] A. Marquina, *Local piecewise hyperbolic reconstructions for nonlinear scalar conservation laws.* SIAM J. Sci. Comput. 15, 892-915 (1994)

[42] M. J. McBride and D. R. Zusman, *FrzCD, a methyl-accepting taxis protein from Myxococcus xanthus, shows modulated methylation during fruiting body formation.* J Bacteriol 175(15), 4936-4940 (1993)

[43] T. Mignot, J. Merlie and D. Zusman, *Regulated Pole-to-Pole Oscillations of a Bacterial Gliding Motility Protein* Science 310 (5749), 855-857 (2005)

[44] J. D. Murray, *Mathematical Biology.* 3rd ed. Springer, New York (2002)

[45] J. D. Murray, *Mathematical Biology II. Spatial models and biomedical applications.* 3rd ed. Springer, Berlin (2003)

[46] S. J. Osher and S. Chakravarty, *High resolution schemes and the entropy condition.* SIAM J. Numer. Anal. 21, 955-984 (1984)

[47] E. Palsson and E. C. Cox, *Origin and evolution of circular waves and spirals in Dictyostelium discoideum territories.* Proc. Natl. Acad. Sci. U.S.A. 93, 1151-1155 (1996)

[48] A. Polezhaev, R. Pashkov, A. Lobanov and I. Petrov, *Spatial patterns formed by chemotactic bacteria Escherichia coli.* Int. J. Dev. Biol. 50, 309-314 (2006)

[49] H. Reichenbach, *The ecology of the myxobacteria.* Environmental Microbiology 1, 15–21 (1999)

[50] E. Rosenberg, K. Keller and M. Dworkin, *Cell density-dependent growth of myxococcus xanthuson casein.* J. Bacteriol. 129, 770-777 (1977)

[51] B. Sager and D. Kaiser, *Intercellular C-signaling and the traveling waves of Myxococcus.* Genes & Dev. 8 (23), 2793-2804 (1994)

[52] T. Sekimura, S. Noji, N. Ueno and P. K. Maini (eds), *Morphogenesis and Pattern Formation in Biological Systems: Experiments and Models.* Springer, Tokyo (2003)

[53] S. Serna, *A class of extended limiters applied to piecewise hyperbolic methods.* SIAM J. Sci. Comput. 28, 123-140 (2006)

[54] S. Serna and A. Marquina, *Power ENO Methods: a fifth-order accurate Weighted Power ENO method.* J. Comput. Phys. 194, 632-658 (2004)

[55] L. J. Shimkets, M. Dworkin and H. Reichenbach, *The myxobacteria*, in The Prokaryotes, vol. 7, edited by M. Dworkin, S. Falkow, E. Rosenberg, K. H. Schleifer, and E. Stackebrandt, Springer, New York, 31-115 (2006)

[56] C. W. Shu and S. J. Osher, *Efficient implementation of essentially non-oscillatory schemes.* J. Comput. Phys. 77, 439-471 (1988)

[57] C. W. Shu and S. J. Osher, *Efficient implementation of essentially non-oscillatory shock-capturing schemes II.* J. Comput. Phys. 83, 32-78 (1989)

[58] F. Siegert and C. Weijer, *Spiral and concentric waves organize multicellular Dictyostelium mounds.* Curr. Biol. 5, 937-943 (1995)

[59] O. Sliusarenko, J. Chen and G. Oster, *From Biochemistry to Morphogenesis in Myxobacteria.* Bulletin of Mathematical Biology 68, 1039-1051 (2006)

[60] O. Sliusarenko, J. Neu, D. Zusman and G. Oster, *Accordion waves in Myxococcus xanthus.* Proc. Natl. Acad. Sci. USA 103, 1534-1539 (2006)

[61] O. Sliusarenko, D. R. Zusman and G. Oster, *Aggregation during Fruiting Body Formation in Myxococcus xanthus Is Driven by Reducing Cell Movement.* Journal of Bacteriology 189(2), 611-619 (2007)

[62] O. Sozinova, Y. Jiang, D. Kaiser and M. Alber, *A three-dimensional model of myxobacterial aggregation by contact-mediated interactions.* Proc. Natl. Acad. Sci. 102, 11308-11312 (2005)

[63] O. Sozinova, Y. Jiang, D. Kaiser and M. Alber*, A three-dimensional model of myxobacterial fruiting-body formation.* Proceedings of the National Academy of Sciences of the United States of America 103, 17255 (2006)

[64] J. Starruß, T. Bley, L. Søgaard-Andersen and A. Deutsch, *A New Mechanism for Collective Migration in Myxococcus xanthus.* Journal of Statistical Physics 128(1), 269-286 (2007)

[65] A. Stevens, *A Stochastic Cellular Automaton Modeling Gliding and Aggregation of Myxobacteria.* SIAM Journal on Applied Mathematics 61, 1, 172-182 (2000)

[66] A. Turing, *The chemical basis of morphogenesis.* Phil. Trnas. R. Acad. Sci. B 237, 37-72 (1952)

[67] J. J. Tyson, K. A. Alexander, V. S. Manorajan and J. D. Murray, *Cyclic AMP waves during aggregation of Dictyostelium amoebae.* Development 106, 421-426 (1989)

[68] R. Welch and D. Kaiser, *Cell behavior in traveling wave patterns of myxobacteria.* PNAS 98 (26), 14907-14912 (2001)

[69] C. Wolgemuth, E. Hoiczyk, D. Kaiser and G. Oster, *How myxobacteria glide.* Curr. Biol. 12, 369-377 (2002)

[70] Y. Wu, Y. Jiang, D. Kaiser and M. Alber, *Social interactions in Myxobacterial swarming.* PLoS Comput Biol 3, e253 (2007)

[71] Y. Wu, D. Kaiser, Y. Jiang and M. S. Alber, *Periodic reversal of direction allows Myxobacteria to swarm*. Proc. Natl. Acad. Sci. 106, 1222-1227 (2009)

[72] H. Zhang, Z. Vaksman, D. Litwin, P. Shi, H. Kaplan and O. A. Igoshin, *The Mechanistic Basis of Myxococcus xanthus Rippling Behavior and Its Physiological Role during Predation*. PLoS Comp. Biology 8, e1002715 (2012)